River Mixing in the Amazon as a Driver of Concentration-Discharge Relationships

Julien Bouchez, Jean-Sébastien Moquet, Jhan Carlo Espinoza, Jean-Michel Martinez, Jean-Loup Guyot, Christelle Lagane, Naziano Filizola, Luis Noriega, Liz Hidalgo Sanchez, Rodrigo Pombosa

AGU PUBLICATIONS

Water Resources Research

RESEARCH ARTICLE
10.1002/2017WR020591

Special Section:
Concentration-discharge Relations in the Critical Zone

River Mixing in the Amazon as a Driver of Concentration-Discharge Relationships

Julien Bouchez[1], Jean-Sébastien Moquet[1,2], Jhan Carlo Espinoza[3], Jean-Michel Martinez[2], Jean-Loup Guyot[2], Christelle Lagane[2], Naziano Filizola[4], Luis Noriega[5], Liz Hidalgo Sanchez[6], and Rodrigo Pombosa[7]

[1]Institut de Physique du Globe de Paris - Centre National de la Recherche Scientifique - Sorbonne Paris Cité, Paris, France, [2]Géosciences Environnement Toulouse, GET/OMP, CNRS/IRD/Université Paul Sabatier, Toulouse, France, [3]Instituto Geofísico del Perú, Lima, Peru, [4]LAPA (Laboratório de Potamologia da Amazônia – Universidade Federal do Amazonas), Av. General Rodrigo Octávio Jordão Ramos 3000, Campus Universitário, Bloco Arthur Reis, Coroado, Manaus, Brazil, [5]SENAMHI Calle Reyes Ortiz no. 41 2do Piso, La Paz, Bolivia, [6]Université Pierre et Marie Curie, Paris, France, [7]INAMHI Iñaquito N36-14 y Corea, Código 16-310, Quito, Ecuador

Key Points:
- Modeling predicts that tributary mixing should affect river concentration-discharge relationships, especially in large, heterogeneous basins
- In the Amazon basin river concentration-discharge relationships of heterogeneous basins are the least "chemostatic"
- Concentration-discharge relationships in large systems are strongly affected by mixing between waters following different pathways

Supporting Information:
- Supporting Information S1
- Figure S1
- Table S1
- Table S2

Correspondence to:
J. Bouchez,
bouchez@ipgp.fr

Citation:
Bouchez, J., Moquet, J.-S., Espinoza, J. C., Martinez, J.-M., Guyot, J.-L., Lagane, C., . . . Pombosa, R. (2017). River mixing in the Amazon as a driver of concentration-discharge relationships. *Water Resources Research*, *53*, 8660–8685. https://doi.org/10.1002/2017WR020591

Received 16 FEB 2017
Accepted 1 SEP 2017
Accepted article online 12 SEP 2017
Published online 2 NOV 2017

Abstract Large hydrological systems aggregate compositionally different waters derived from a variety of pathways. In the case of continental-scale rivers, such aggregation occurs noticeably at confluences between tributaries. Here we explore how such aggregation can affect solute concentration-discharge (*C-Q*) relationships and thus obscure the message carried by these relationships in terms of weathering properties of the Critical Zone. We build up a simple model for tributary mixing to predict the behavior of *C-Q* relationships during aggregation. We test a set of predictions made in the context of the largest world's river, the Amazon. In particular, we predict that the *C-Q* relationships of the rivers draining heterogeneous catchments should be the most "dilutional" and should display the widest hysteresis loops. To check these predictions, we compute 10 day-periodicity time series of *Q* and major solute (Si, Ca^{2+}, Mg^{2+}, K^{+}, Na^{+}, Cl^{-}, SO_4^{2-}) *C* and fluxes (*F*) for 13 gauging stations located throughout the Amazon basin. In agreement with the model predictions, *C-Q* relationships of most solutes shift from a fairly "chemostatic" behavior (nearly constant *C*) at the Andean mountain front and in pure lowland areas, to more "dilutional" patterns (negative *C-Q* relationship) toward the system mouth. More prominent *C-Q* hysteresis loops are also observed at the most downstream stations. Altogether, this study suggests that mixing of water and solutes between different flowpaths exerts a strong control on *C-Q* relationships of large-scale hydrological systems.

1. Introduction

The release of solutes to rivers by chemical weathering results from water-rock interactions. Weathering models account for these interactions by coupling laws for mineral precipitation and dissolution with water transport (Goddéris et al., 2006; Steefel et al., 2005) or by assuming a direct dependency of weathering fluxes on water fluxes (linear as in Berner et al., 1983; or nonlinear as in Bluth and Kump, 1994) or on water residence time in the system (Maher, 2010). Conversely, empirical observations on the relationship between solute export and water fluxes, as a function of time or across different catchments, may provide insight into weathering mechanisms and coupling between hydrology and water-rock interactions in the Critical Zone (Calmels et al., 2011; Clow & Mast, 2010; Eiriksdottir et al., 2013; Godsey et al., 2009; Ibarra et al., 2016; Maher & Chamberlain; 2014; Maher, 2011; Torres et al., 2015; Von Blanckenburg et al., 2015).

The instantaneous solute export (*F*, e.g., in $mol.s^{-1}$) from a watershed is equal to discharge (hereafter termed *Q*, e.g., in $L.s^{-1}$) times solute concentration (hereafter referred to as *C*, e.g., in $mol.L^{-1}$):

$$F = C.Q \tag{1}$$

As these two metrics can be readily measured, and even possibly measured at a relatively high frequency (Floury et al., 2017), relationships between *Q* and *C* through time ("*C-Q* relationships") have long been a focus of characterization in hydrology (Anderson et al., 1997; Meybeck, 1976; Saunders & Lewis, 1989) - one

practical interest of this approach being to establish rating curves to estimate C based on Q time series, which benefit usually from a much higher measurement frequency.

From a theoretical perspective, two extreme scenarios can *a priori* be distinguished for a given C-Q relationship: one where the release of solute from the watershed, F, is constant, and concentrations C vary following a dilution law, i.e., as Q^{-1}; and one where C is constant, and where F scales as Q. The interest in C-Q relationships has been recently revived by Godsey et al.'s (2009) analysis of data from small basins of the US Hydrology Benchmark Network (HBN), suggesting that these end members are best expressed through the functional fit of C-Q relationships by a power law:

$$C = a.Q^b \tag{2}$$

where a and b are the fit parameters. Godsey et al. (2009) coined the term "chemostatic" to describe that for most solutes the power law exponent b is close to 0, i.e., that many small rivers display a limited variability in C compared to that in Q. This observation has two main implications: (1) through time, F depends primarily on Q; (2) a mechanism is at play in the Critical Zone, "buffering" variations in C against dilution. To examine the possible mechanism that could account for their observation of the chemostatic behavior of river catchments, Godsey et al. (2009) reviewed a set of previous models (Johnson et al., 1969; Langbein & Dawdy, 1964) and suggested a new "porosity-permeability-aperture model" ("PPA model"), deemed plausible and featuring only measurable field parameters, and therefore testable.

The "initial chemostatic observation" of Godsey et al. (2009) has since been refined, in particular by Maher (2011) who included the trend toward dilution usually observed at high Q (Bluth & Kump, 1994). Maher (2010, 2011) indeed introduced a 1D-reactive transport model based on a 1st-order dependency of solute production on C (i.e., F scaling with C - C_{eq}, where C_{eq} is the solute concentration at chemical equilibrium), yielding:

$$C = C_0 e^{-Dw/q} + C_{eq}\left(1 - e^{-Dw/q}\right) \tag{3}$$

where Dw is the Damköhler coefficient, that depends on the rate of solute release from minerals, flowpath length, and C_{eq} (Maher & Chamberlain, 2014). This model has been used recently by Ibarra et al. (2016) to retrieve the Dw values of monolithological, relatively small basaltic and granitic catchments throughout the world based on their individual C-Q relationships, and infer the difference in weatherability between these two rock types.

Other recent studies at a larger scale have shown that power law fits of C-Q relationships could yield b-values significantly lower than 0 (Moon et al., 2014; Moquet et al., 2016; Torres et al., 2015). In particular, using a series of four nested catchments in the upper Madre de Dios basin (southwestern Amazon basin), Torres et al. (2015) observed a systematic decrease of the b-value with basin altitude for most solutes, with a more chemostatic behavior in mountainous basins and a larger effect of dilution at lowland locations. Based on the framework introduced by Maher (2011), this was chiefly interpreted as a change in the weathering efficiency from mountainous regions, with shorter surface water residence time and more altered regolith leading to decreased weathering efficiency in lowland regions compared to mountains (Torres et al., 2015).

River catchments are complex and heterogeneous systems, be it regarding water (rainfall) and element inputs (e.g., atmospheric wet and dry inputs, weathering, or anthropogenic contamination), or in terms of other parameters that might influence the motion of water and elements (e.g., soil depth and type, or vegetation cover). Although the recent body of work on C-Q relationships has yielded significant insight into the links between water flow and solute export in weathering systems, interpretation of C-Q relationship has until now heavily relied on a strong assumption: namely that the whole area upstream the sampling point is homogenous in terms of properties that are relevant to the interpretation (with the notable exception of the inclusion of water travel time distributions by Maher, 2011). The issue of environmental heterogeneity and aggregation of different flowpaths has recently been addressed by Kirchner (2016a, 2016b), who showed in particular how such heterogeneity strongly affects any inference that can be made on water travel time distribution from C and Q time series.

One feature that has been overlooked in the most recent analyses of C-Q relationships is the presence of hysteresis loops, although its existence has been long recognized (e.g., Evans & Davies, 1998; Hornberger

et al., 2001; House & Warwick, 1998; Rose, 2003). Besides a handful of studies (e.g., Duffy & Cusumano, 1998), *C-Q* loops have often been interpreted as an offset between the discharge of different hydrological reservoirs within a given catchment (e.g., surface water, soil water, groundwater; e.g., Calmels et al., 2011; Edokpa et al., 2015) or, when observed downstream from a confluence, between tributaries (Ollivier et al., 2006; Moquet et al., 2016). Therefore, there seems to be a general agreement that environmental heterogeneity should generate hysteresis in *C-Q* relationships. However, we still lack systematic observations and theoretical frameworks about *C-Q* hysteresis loops, as well as potential links between these loops and other features of *C-Q* relationships, especially in large, heterogeneous river systems.

In the present paper we examine how catchment heterogeneity affects *C-Q* relationships, through the time-varying contribution of different subcatchments. In large watersheds, the process of aggregation of water pathways is easy to pinpoint as it occurs mostly at confluences of tributaries. In particular, we explore the hypothesis that previously observed changes in *b*-values with catchment size catchment could stem solely from aggregation of heterogeneous subcatchments, as large drainage areas are more likely to collect water and solutes fluxes that drastically differ in timing and amplitude of temporal variations. To that effect, we build up a simple model of water and solute mixing from two compositionally different, chemostatic tributaries, which predicts the trend (*b*-value) and shape (hysteresis loops) of *C-Q* relationships in the mixed water flow, depending on the differences between the two tributaries in terms of solute concentration, variation of discharge, and timing of peak discharge. We then turn toward the Amazon basin to check these predictions. The Amazon, which is the largest river basin in the world, is well suited for this approach as its tributaries drain areas that greatly differ in climate, lithology, or geomorphic characteristics. Altogether, our study questions the inferences that can be made on *C-Q* relationships about the properties of weathering systems, beyond a certain spatial scales and a certain degree of aggregation of water pathways.

2. Study Area

The Amazon basin is the largest fluvial basin in the world with a drainage area of about 5.9 million km^2 (Callède et al., 2010), located in the tropical region between 5°16′N and 20°28′S and between 79°36′W and 50°15′W, from the Andes to the tropical Atlantic Ocean. It contributes to 16–18% of the continental discharge (Dai & Trenberth, 2002; Callède et al., 2010) and to around 7% of the flux of dissolved species to the ocean (Moquet et al., 2016).

The Amazon has 5 main tributaries (Figure 1). The Negro River drains the Brazilian Shield in the northern Amazon; the Solimões River drains the Northern and Central Andes and a large part of the Lowlands; the Madeira River drains the Southern Andes, the Southern Foreland basins and part of the Brazilian shield; and the Tapajós and Xingu drain the remaining area of the Brazilian shield.

The basin receives around 2,200 $mm.yr^{-1}$ of precipitation (Espinoza et al., 2009a) resulting in a mean discharge of 206,000 $m^3.s^{-1}$ (Callède et al., 2010). The climate is monsoonal and is mainly controlled by the seasonal variation of the Southern American Monsoon System (SAMS) throughout the north-south oscillation of the Intertropical Convergence Zone (ITCZ) (Marengo et al., 2012; Vera et al., 2006). While the northwestern part of the basin receives a high amount of rainfall around the year, generally up to 3,000 $mm.yr^{-1}$, the drier part of the basin is located in the southern Andes, where semiarid conditions can be met, particularly during the austral winter (dry season). However, over the Andean region, interactions between the topography and the atmospheric circulation produce a strong rainfall gradient that can vary from 6,000 to 300 $mm.yr^{-1}$ over a few kilometers (Espinoza et al., 2015). The North-South annual rainfall gradient is linked to a gradient in the seasonality of rainfall. In the northern wetter region of the basin, the seasonality is low and, the Seasonal Variability Coefficient (SVC) is generally above 0.3. Conversely, in the southern, drier region of the basin, the seasonality is strongly marked with a SVC of up to 0.8 (Espinoza et al., 2009a). This seasonal variability of rainfall distribution implies that the discharge of the rivers is variably marked by seasonality. An offset of the maximum of discharge is also observed between the main Amazon tributaries according to the evolution of the position of the ITCZ and the SAMS intensity along the year (Espinoza et al., 2009b). Therefore, along the year, the maximum of discharge is first recorded in the southeastern and southern basins (Tapajós and Madeira rivers), then in the central and western basins (Solimões River) and finally in the northern basins (Negro River). This hydroclimatic gradient is therefore a first cause for heterogeneity in water and solute fluxes across the Amazon basin (Figure 1b).

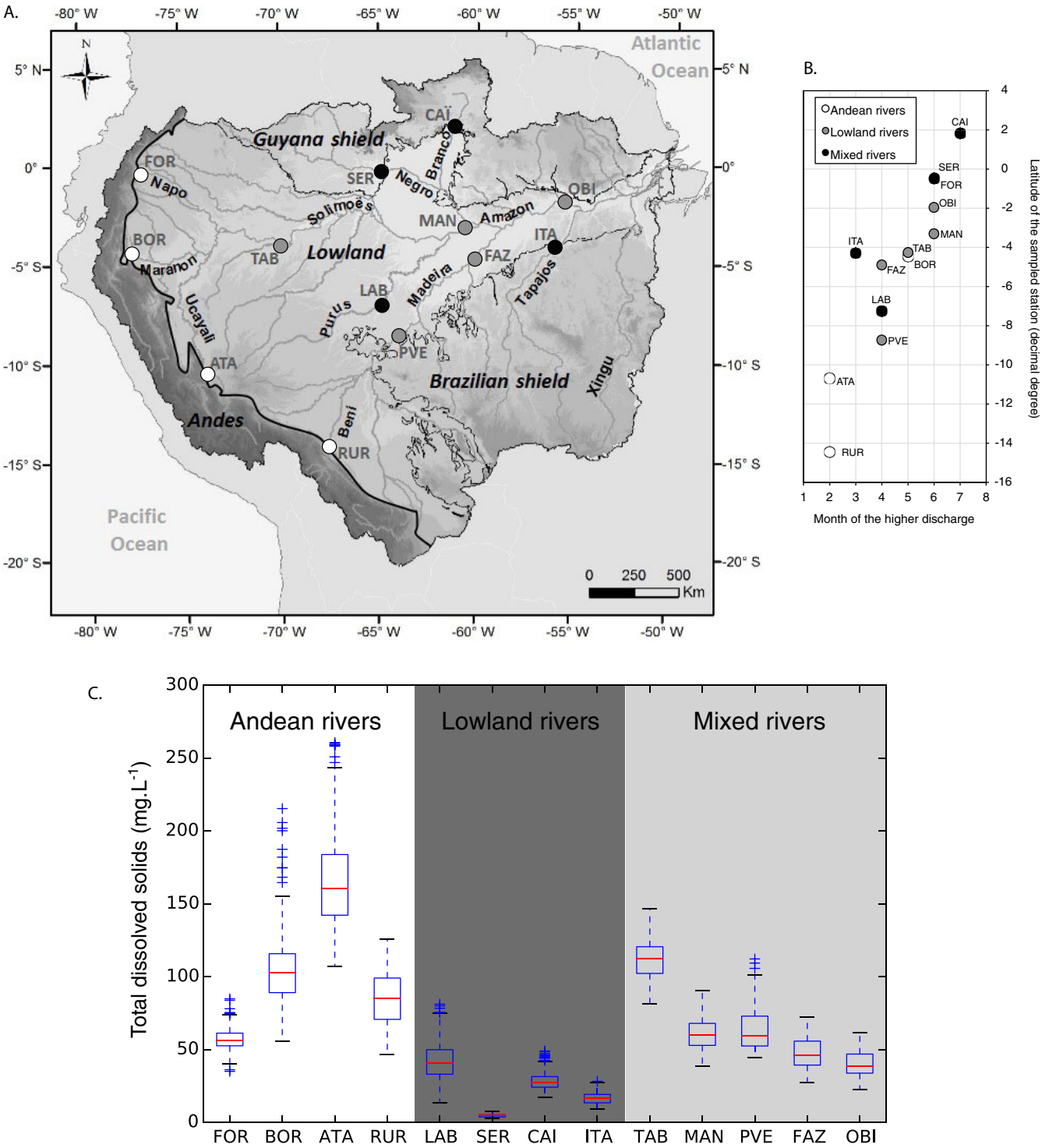

Figure 1. (a) Topographic map of the Amazon basin, gauging stations of the HYBAM network, and main geomorphic domains. The location of the Andean front (defined as the contour line of the 500 m-a.s.l.) is shown as a thick black line. (b) Time of peak discharge in the year versus latitudinal coordinate for the studied gauging stations. (c) Box-plot of the distribution of total dissolved solids (sum of major species concentration, including HCO_3^-) for the 13 gauging stations of our database, ranked following their geomorphic context. This plot shows the major difference between solute-rich, Andean rivers and dilute Lowland waters. The red line is the median of the distribution, the box limits are the upper and lower quartile, the whiskers delimit the data range and crosses are outliers (as defined by the Python *matplotlib boxplot* function). In panels A and B, stations corresponding to Andean rivers, pure lowland rivers, and mixed rivers are indicated as white, black, and gray circles, respectively.

This diversity of geologic and climatic characteristic throughout the Amazon basin generates a strong gradient in erosion and weathering regimes, which in turn affects the quality of the water transported by rivers (Figure 1c). Rivers draining the Andes (among which the main tributaries, from south to north: the Mamoré, Beni and Madre de Dios - draining to the Madeira River -, Ucayali, Huallaga, Marañón and Napo - draining to the Solimões River) are typical of the "white waters" (Gibbs, 1967; Ríos-Villamizar et al., 2014; Sioli, 1964), i.e., characterized by high dissolved concentrations and fluxes. Solute fluxes are high (172.10^6 t.yr^{-1}) in the Andes (Gaillardet et al., 1997, Moquet et al., 2011, 2014a, 2016; Sanchez et al., 2015). This area contributes to nearly 100% and to around 64% of the Amazon solid and solute annual exports, respectively. In particular, this region supplies most of Na^+, Ca^{2+}, Mg^{2+}, Cl^-, SO_4^{2-} to the system (Moquet et al., 2016). By contrast, in the Shields and the Lowlands, solute fluxes are relatively low (Moquet et al., 2016; Wittmann et al., 2011). The Shields are drained by "black water"-type rivers (such as the Negro River), with high organic matter content reflecting intense weathering processes in strongly cation-depleted regolith, such as podzolization; or "clear water"-type rivers (such as the Tapajós, Trombetas or Branco rivers), with high primary productivity (Gaillardet, 1997; Gibbs, 1967; Sioli, 1964). With solute fluxes of less than 30.10^6 t.yr^{-1}, respectively (Moquet et al., 2016), these rivers contribute to less than 10% of the Amazon annual fluxes. Finally, rivers draining the low-standing areas of the Lowlands regions are of the clear-water or black-water type (Ríos-Villamizar et al., 2014) with low solute loads (Stallard & Edmond, 1983). With solute fluxes of about 70.10^6 t.yr^{-1}, Lowlands contribute to a minor yet significant part of the solute fluxes of the Amazon (Moquet et al., 2016). Therefore, hydrochemistry varies significantly between the different geomorphic domains across the Amazon Basin, in particular between the Shield and the Lowlands (Figure 1c). Altogether, the hydroclimatic and hydrochemical heterogeneity of the Amazon Basin make it a natural laboratory where the behaviour of *C-Q* relationships at downstream stations should be significantly influenced by mixing of waters from different tributaries.

The anthropogenic influence across the Amazon is limited, although large dams are being built on the Madeira River (Latrubesse et al., 2017), and mining activity exists in the Andes and in the Shield areas. We also note that a significant release of Na^+ and Cl^- to the rivers through the exhumation of brines during oil exploration has been observed between 2007 and 2009 on the Marañón River, affecting even the Amazon at its mouth (Moquet et al., 2014b).

In the context of the Amazon Basin, a variety of hydrological, inorganic and biological processes have been invoked to explain observed *C-Q* relationships. With increasing *Q*, the dilution of Cl^- delivered by evaporite dissolution in the Andes (Moquet et al., 2016) or by inputs of deep water through oil extraction in the Peruvian foreland (Moquet et al., 2014b), has been attributed to a constant Cl^- release flux superimposed on variable water discharge. Conversely, nearly constant concentrations along the hydrological cycle have been explained by sorption processes, for example, for PO_4^{3-} in the Solimoes basin (Devol et al., 1995), or by thermodynamic equilibrium between soils or suspended matter and water for K and Si for most of the Amazon subbasins (Moquet et al., 2016). Finally, for some elements concentrations increase with discharge, as is the case, for example, for PO_4^{3-} or NO_3^- in a small watershed in Ecuador (Boy et al., 2008) which was attributed to the mobilization of matter from the soil surface by runoff during rain events. This behavior is also observed for major elements in rivers draining Shield areas (Markewitz et al., 2001) or in some basins of the Andean headwater of the Madeira Basin (Guyot, 1993; Roche & Fernandez, 1988). In both cases, the authors suggested that solutes are released by weathering of surficial soil layers within the catchment during high runoff periods. In some rivers, *C-Q* relationships shift significantly over the hydrological period: for example, in the Beni basin Guyot (1993) and Moquet et al. (2016) reported a dilutional behavior of major elements during the dry season and an increase of solute concentration with *Q* during the wet season, which was explained by the contrasted hydrological regimes between the dry and wet seasons in this semiarid context (Roche & Fernandez, 1988).

3. Data Source and Processing

3.1. Database for Concentration and Discharge

We used the SNO-HYBAM (Geodynamical, hydrological, and biogeochemical controls on erosion/weathering and material transport in the Amazon, Orinoco, and Congo basins) observatory discharge and chemical data recorded at 13 hydrological stations between 2003 and 2008. These stations are located on the four

Table 1
Description of the Gauging Stations of the HYBAM Network Used in This Study

Geomorphological domain	Hydrosystem	River	Station name	Full name	Upstream stations inputs	Geographic coordinates X (°)	Geographic coordinates Y(°)	Annual discharge (10^3 $m^3.s^{-1}$)	Drainage area (10^3 km^2)	% basin in the Andes (>500m)	Water sampling period
Andes	Solimões	Napo	FOR	Francisco de Orellana		−76.98	−0.474	1.2	12	69%	2000–2008
	Solimões	Upper Maranon	BOR	Borja		−77.55	−4.47	5	114	91%	2003–2008
	Solimões	Ucayali	ATA	Atalaya-Lagarto		−73.82	−10.68	7	191	87%	2003–2008
	Madeira	Beni	RUR	Rurrenabaque		−67.53	−14.44	2	70	92%	2003–2008
Lowland	Solimões	Purus	LAB	Labrea		−64.8	−7.252	5.5	226	0%	2004–2008
	Negro	Upper Negro	SER	Serrinha		−64.83	−0.497	17	290	0%	2003–2008
	Negro	Branco	CAI	Caracaraï		−61.12	1.819	3.6	125	0%	2003–2008
	Tapajós	Tapajós	ITA	Itaituba		−55.98	−4.283	12	458	0%	2004–2008
Mixed	Solimões	Amazonas/ Solimoes	TAB	Tabatinga	FOR + BOR + ATA	−69.96	−4.242	35	877	46%	2003–2008
	Solimões	Solimoes	MAN	Manacapuru	TAB + LAB	−60.55	−3.345	102	2203	19%	2003–2008
	Madeira	Madeira	PVE	Porto Velho	RUR	−63.92	−8.788	18	978	21%	2003–2008
	Madeira	Madeira	FAZ	Fazenda Vista Alegre	PVE	−60.03	−4.897	26	1314	15%	2003–2008
	Amazon	Amazon	OBI	Óbidos	MAN + FAZ + SER + CAI	−55.51	−1.947	177	4671	13%	2003–2008

main Amazon tributaries (Negro, Solimões, Madeira and Tapajós rivers), corresponding to drainage areas between 12 and 4,671.10^3 km^2 (Table 1) and categorized in three main river types: Andean, Lowland, and mixed rivers (typically downstream stations) (Figure 1). Hydrological data have been produced using conventional hydrological methods. Water levels were recorded daily or twice daily, and the daily discharge series was calculated from rating curves (discharge versus water level) based on 3-months frequency gauging using a 600 kHz (Peru, Bolivia and Brazil) or 1,200 kHz (Ecuador) Acoustic Doppler Current Profiler (ADCP). For hydrochemical data, only major elements (Cl^-, SO_4^{2-}, Na^+, Ca^{2+}, Mg^{2+}, K^+) have been considered in the present study. Hydrogenocarbonate ion (HCO_3^-), although a major dissolved component of river waters, has not been considered in the present study as its dynamics can be largely controlled by gaseous exchange (e.g., Abril et al., 2014). A sample of 650 mL was collected monthly at each gauging station. The samples were filtered on site using a 0.2-μm porosity filter. Concentrations were determined at the GET laboratory (Géoscience Environnement Toulouse, France) for Ecuadorian, Peruvian and Bolivian samples and at the "Instituto de Geociencias" laboratory of the Universidade de Brasilia (UnB) for Brazilian samples. The samples were analyzed according to the procedure described in Cochonneau et al. (2006). Cl^- and SO_4^{2-} concentrations were measured by ion chromatography, and Na^+, Ca^{2+}, Mg^{2+}, K^+ and Si were analyzed by ICP-AES (Inductively Coupled Plasma-Atomic Emission Spectroscopy). Based on the analyses of geostandards, the analytical error is less than 10%.

3.2. Computation of Time Series

Daily discharge and monthly hydrochemical data were downloaded from the SNO-HYBAM website (http://www.ore-hybam.org). Using the HYDRACESS software (Vauchel, 2005), a 10 day periodicity time series was produced for each station and each parameter, for *Q* by averaging 10 daily data points and for *C* by linear interpolation of the monthly original time series. This allows for having synchronous *C* and *Q* databases. The validity of a linear interpolation of *C* from the monthly to the 10 day periodicity is justified by the relatively smooth temporal variations of *C*, and the weak contribution of high-frequency variation in the power density spectra (see supporting information section S1).

In this paper, in addition to using *Q* and *C* times series, we rely on temporal variations of solute fluxes *F*. In the scope of the present work, *F* has two interesting properties:

1. Like *Q* and unlike *C*, *F* can - under certain conditions - be additive during aggregation of water pathways and therefore fullfill simple mass balance requirements. For example, the sum of the input fluxes of a

Table 2
Mean Discharge (Q) *and Solute Flux (F) and Corresponding Relative Standard Deviation (s.d.) for Each Station and Solute*

	Discharge		Si		SO_4^{2-}		Cl^-		Na^+		K^+		Mg^{2+}		Ca^{2+}	
	Mean ($m^3.s^{-1}$)	s.d. (%)	Mean ($kg.s^{-1}$)	s.d. (%)	Mean ($kg.s^{-1}$)	s.d. (%)	Mean ($kg.s^{-1}$)	s.d. (%)	Mean ($kg.s^{-1}$)	s.d. (%)	Mean ($kg.s^{-1}$)	s.d. (%)	Mean ($kg.s^{-1}$)	s.d. (%)	Mean ($kg.s^{-1}$)	s.d. (%)
FOR	1314	36	9.3	38	3.5	38	0.7	52	3.3	39	1.9	38	1.5	37	10	37
BOR	5045	34	27	51	48	41	17	37	21	36	5.2	50	11	47	97	56
ATA	5770	59	29	59	151	50	54	51	50	55	8.8	64	22	52	153	61
RUR	1998	80	7.8	92	41	77	1.6	49	6.1	70	2.3	93	6.8	74	19	78
LAB	5805	69	38	89	15	80	2.8	90	9.9	70	6.6	68	6.4	64	31	63
SER	17245	38	30	39	8.8	122	4.2	80	14	165	7.3	103	2.7	57	8.4	54
CAI	3496	80	21	70	2.7	173	2.7	87	8.1	78	5.3	86	2.8	80	5.8	79
ITA	12619	61	50	59	3.5	76	6.8	71	9.4	63	11	69	6.2	51	18	72
TAB	35844	30	214	52	291	44	282	47	298	37	46	36	84	33	732	35
MAN	105504	28	447	26	412	32	390	26	364	31	98	31	138	28	1008	31
PVE	17850	66	85	76	169	57	15	129	43	62	28	74	42	60	133	66
FAZ	27011	67	114	70	169	60	21	76	61	66	36	74	45	61	126	60
OBI	186330	29	782	30	474	42	345	20	384	17	163	27	185	28	1038	26

given *conservative* solute by two tributaries at a confluence is equal to the flux of the same element in the mainstream after the confluence, whereas this is not true for *C*. We emphasize that having additive *F* requires that the solute is conservative during mixing (Guinoiseau et al., 2016) and that the downstream *F* is calculated taking into account potential lateral heterogeneity in the channel (Bouchez et al., 2010). Spectral analysis tools such as Fourier transform can then also be applied to an additive parameter such as *F*, in order to retrieve the properties of water transport systems (see section 5.1).

2. As *C* variations are not as strong as *Q* variations in the Amazon (Moquet et al., 2016, and this study), *F* is strongly controlled by *Q*, such that *F* variations are as easy to characterize empirically as *Q* variations, which might not be the case for *C* variations (see e.g., the case of sine-wave fits in supporting information section S2).

Therefore, 10 days frequency *F* records were computed by multiplication of the 10 days frequency *Q* and *C* records (equation (2)). Mean *Q*, *C*, and *F* values, along with relative standard deviations, are provided in Tables 2 and 3. In this scope we note that the inferred standard deviations in *Q* depend on the frequency of the *Q* record used (calculations not shown here, but performed for periods between 1 day and 1 month from the HYBAM database).

Table 3
Mean Solute Concentration (C) *and Corresponding Relative Standard Deviation (s.d.) for Each Station and Solute*

	Discharge		Si		SO_4^{2-}		Cl^-		Na^+		K^+		Mg^{2+}		Ca^{2+}	
	Mean ($m^3.s^{-1}$)	s.d. (%)	Mean ($mg.L^{-1}$)	s.d. (%)	Mean ($mg.L^{-1}$)	s.d. (%)	Mean ($mg.L^{-1}$)	s.d. (%)	Mean ($mg.L^{-1}$)	s.d. (%)	Mean ($mg.L^{-1}$)	s.d. (%)	Mean ($mg.L^{-1}$)	s.d. (%)	Mean ($mg.L^{-1}$)	s.d. (%)
FOR	1314	36	7.1	14	2.7	22	0.6	41	2.6	25	1.5	16	1.2	23	7.7	18
BOR	5045	34	5.3	29	9.4	23	3.5	39	4.3	32	1	25	2.1	29	18.8	37
ATA	5770	59	5.3	15	31.7	39	12.5	57	10.7	50	1.6	18	4.5	30	28.9	24
RUR	1998	80	4.1	18	25.6	36	1.2	58	3.8	35	1.2	36	4	27	10.7	24
LAB	5805	69	6.6	35	3	59	0.6	65	2.1	42	1.2	28	1.4	42	6.9	43
SER	17245	38	1.8	20	0.7	180	0.2	52	0.8	129	0.4	82	0.2	31	0.5	32
CAI	3496	80	6.4	16	0.8	121	0.8	34	2.5	34	1.5	36	0.8	17	1.6	21
ITA	12619	61	4.2	13	0.3	47	0.7	70	0.8	29	0.9	16	0.6	21	1.4	45
TAB	35844	30	6	34	8.3	40	8.1	41	8.9	40	1.3	15	2.4	20	20.7	18
MAN	105504	28	4.4	11	4.3	39	4.1	41	3.8	33	1	24	1.4	20	10	22
PVE	17850	66	4.7	19	11.1	36	1	60	2.8	37	1.5	15	2.7	30	8.5	34
FAZ	27011	67	4.4	16	7.5	29	1	60	2.9	48	1.4	20	2	28	5.7	31
OBI	186330	29	4.3	27	2.8	50	2.1	42	2.3	36	0.9	28	1	31	5.9	28

3.3. Main Features of the Discharge, Concentration, and Solute Fluxes Records

The water discharge and chemistry of the dissolved load of the Amazon have been reported and interpreted extensively elsewhere (e.g., Gaillardet, 1997), and parts of the present database have been published and discussed in detail in Moquet et al. (2011, 2016). Therefore, in this paper we do not comment extensively on the values taken by Q and C and the contribution of different solutes to the total load. However, we provide here a summary on their variation through time.

Discharge generally increases downstream, with the lowest mean Q of the database recorded for the BOR station (1,314 m^3/s) and the largest for Óbidos (1,86,330 m^3/s; Figure 2 and supporting information Figures S14–S26). The Andean stations have the lowest mean Q of the database (Table 2). Across the record period, Q varies from by 29% (relative standard deviation calculated over all 10 day periodicity data points available) for OBI and by up to 80% for RUR and CAI stations. Some northern Andean stations exhibit a relatively low variability in Q (e.g., around 35% for FOR or BOR), whereas at some of the southern downstream stations, such as PVE of FAZ, Q is much more variable (relative standard deviation $>$ 65%) reflecting the difference in precipitation variability between the two regions (Espinoza et al., 2009b; Molina-Carpio et al., 2017).

At all stations, the C of all considered solutes varies significantly across the period of study (Figure 3 and supporting information Figures S27–S39). In terms of mean concentration values, the species contributing most to the anion mass load is HCO_3^- (not considered in the C-Q analyses in this paper) at all stations, whereas that contributing the most to the cation mass load is Ca^{2+} for most stations (except CAI and SER where it is Na^+). For all solutes with the exception of Si, the highest mean C is measured on the Ucayali River at the ATA station. For Si, the highest mean C is obtained at the Andean station of FOR. The relative variation in mean C across the set of gauging stations is about 30% for all solutes except for Si and K^+, where it is around 20%. Over the period of record, the highest temporal variability in C is generally observed for Cl^- (relative standard deviation: 34–70% depending on the station) and SO_4^{2-} (22–180%), and the lowest for Si (11–35%; Table 3). Nevertheless, we emphasize that the station SER exhibits fairly low average concentration values for all solutes, over which analytical issues (e.g., contamination during sampling, or precision and accuracy of analyses) will have the strongest imprint.

Averaged over all the stations, the highest mean solute flux is recorded for Ca^{2+} (range: 6-1,038 $kg.s^{-1}$) and the lowest for Cl^- (0.7–782.0 $kg.s^{-1}$), Mg^{2+} (1.5–185.4 $kg.s^{-1}$), and K^+ (1.9–162.8 $kg.s^{-1}$; Table 2; Figure 2 and supporting information Figures S14–S26). The stations which record the lowest F are the Andean stations FOR (0.7–9.4 $kg.s^{-1}$ depending on the solute) and RUR (1.6–41.3 $kg.s^{-1}$), due to their relatively small drainage area and thus low Q; and the stations located on the pure lowland rivers SER (4.2–29.8 $kg.s^{-1}$) and CAI (2.7–21.2 $kg.s^{-1}$), due to their dilute nature and thus low C. Depending on the station, the temporal variability in F ranges from 20–30% (relative standard deviation) to 80% (Mg^{2+} at OBI) to 173% (SO_4^{2-} at CAI). There is no systematic difference in variability between different families of rivers: for Andean stations, the variability in F ranges from 37% (Ca^{2+} at FOR) to 93% (K^+ at RUR), whereas for lowland stations, it is between 17% (Na^+ at OBI) and 173% (SO_4^{2-} at CAI).

Therefore, our database encompasses a set of gauging stations located throughout the Amazon Basin, among which three groups can be distinguished: Andean-derived rivers featuring high solute concentrations (FOR, BOR, ATA, RUR), rivers draining only low-relief areas and carrying dilute waters (LAB, SER, CAI, ITA); and rivers draining both Andean and Lowland regions (TAB, MAN, PVE, FAZ, and OBI) (Table 3 and Figure 1). The study of concentration-discharge-fluxes relationships across the Amazon basin thus allows us to address the role of environmental heterogeneity on C-Q relationships, through the aggregation of different types of water.

4. A Model for Nonreactive Mixing of Water and Solutes

4.1. Model Setup and Numerical Experiment

We consider two water flows carried by two theoretical tributaries *1* and *2*, the mixing of which produces a downstream flow (mixture *m*; Figure 4). Discharge (q_1 and q_2) is assumed to vary as a sine wave in each tributary at the same frequency (angular frequency ω), but differs in average (v_1 and v_2), amplitude (w_1 and w_2) and phase (φ_1 and φ_2). We then consider a conservative solute carried by the two tributaries, which are both assumed to be chemostatic (their b-exponent is therefore 0). Therefore, the solute concentration

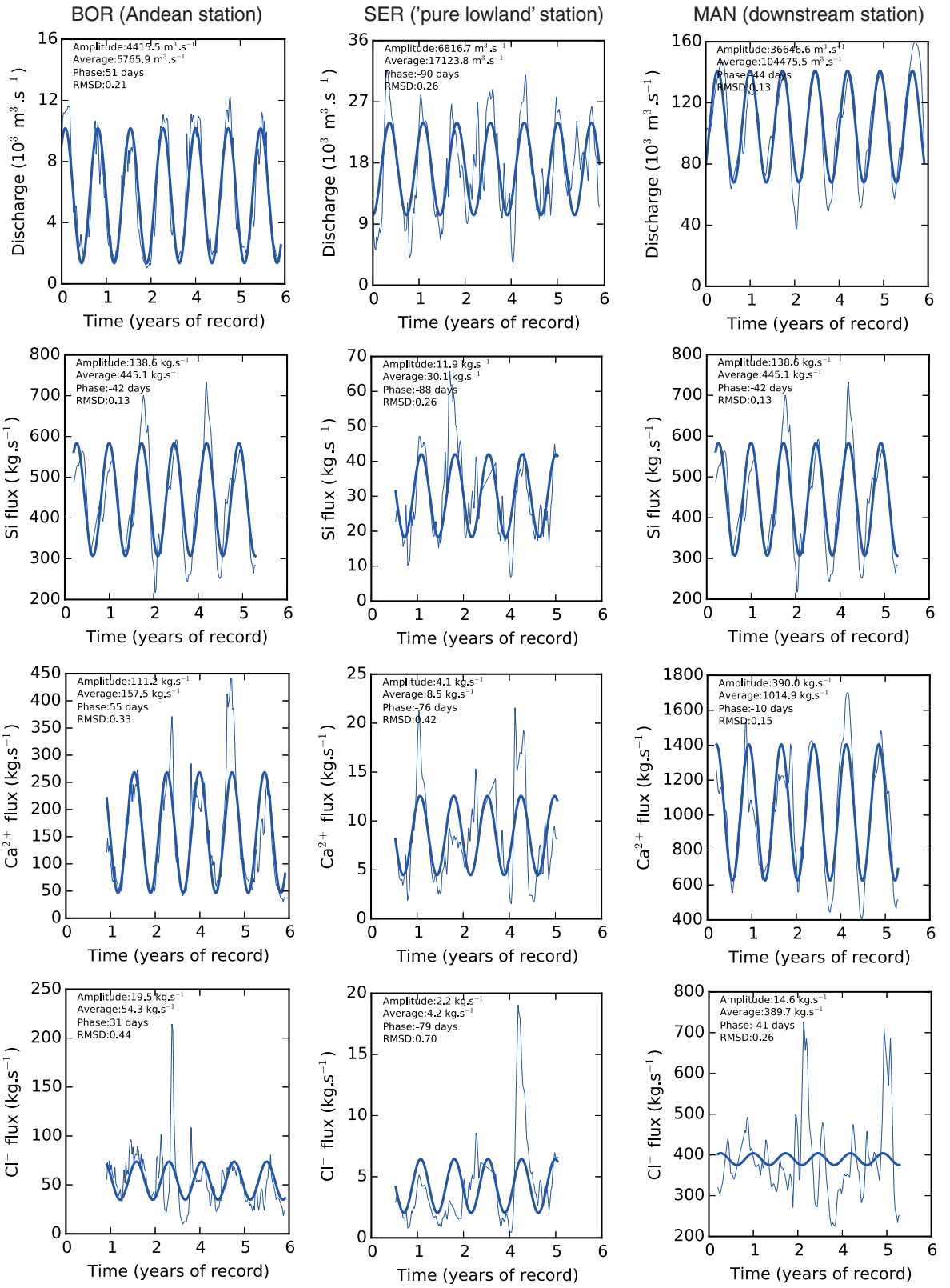

Figure 2. Discharge (*Q*) and solute fluxes (*F*) time series for a selection of gauging stations and solutes. The 10 day period data is presented as a thin blue curve, the sine wave best fit as a thick blue line (see supporting information section S2). The parameters of the best fit (amplitude, mean, and phase), as well as its quality as indexed by the normalized root mean square deviation (*RMSD*) are indicated. The left panels correspond to the Andean station BOR (Marañón); the central panels to the station SER (Negro) that drain only the Amazon Lowlands; and the right plots to the downstream station MAN (Solimões) that represent a mixture of these different types of inputs.

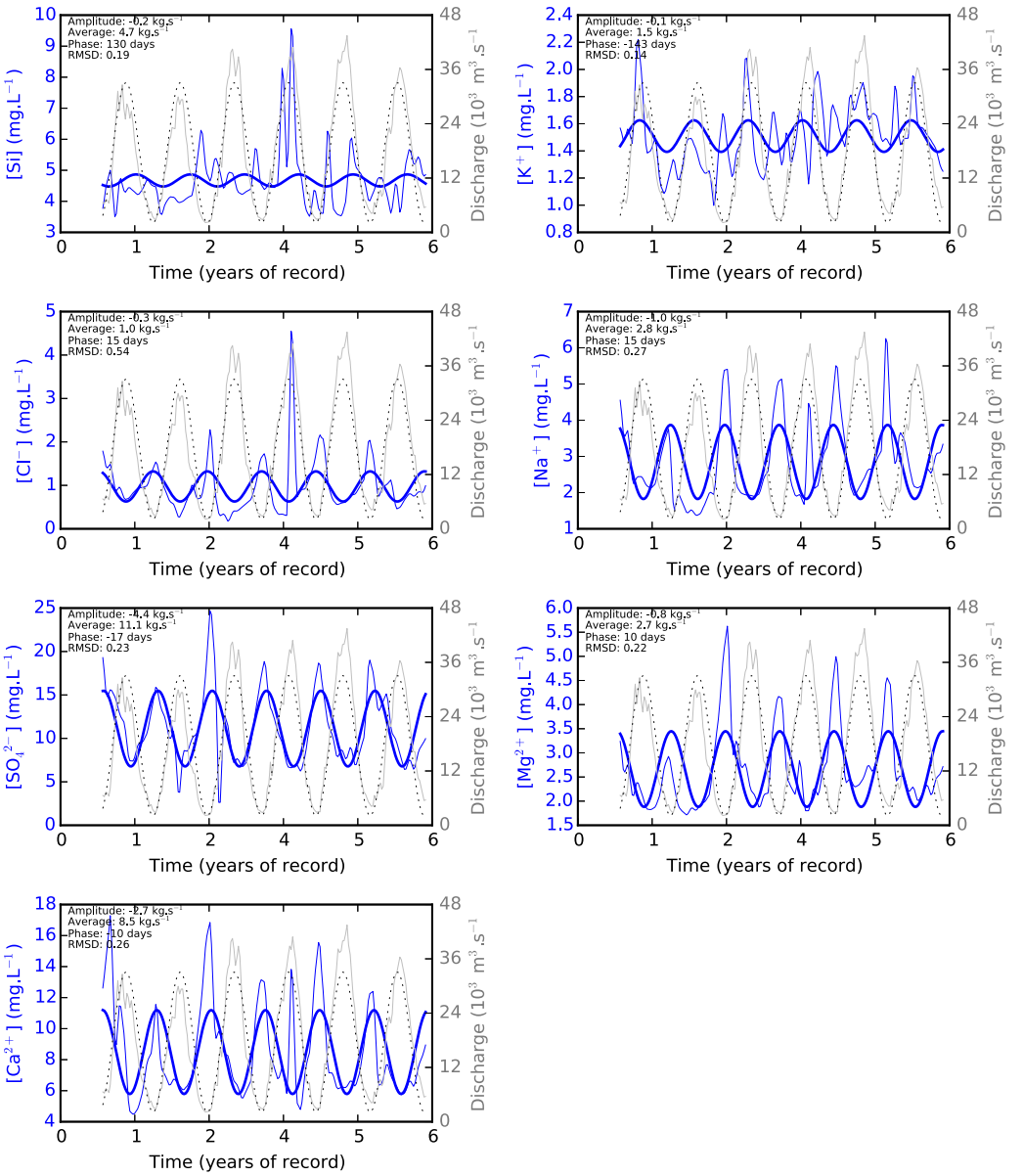

Figure 3. Concentration (*C*) and discharge (*Q*) time series for the station PVE (located on the Madeira River) for the 7 major solutes considered in this study. The 10 day period data is presented as a thin blue curve for *C* and a thin grey curve for *Q*, the sine wave best fit as a thick blue line for *C* and a dotted black line for *Q* (see supporting information section S2). The parameters of the best fits of *F* time series (amplitude, mean, and phase), as well as its quality as indexed by the normalized root mean square deviation (*RMSD*) are indicated.

(C_1 and C_2) in each tributary is constant with time *t*. This is thought to reflect the near-chemostatic behavior of small, homogeneous tributaries (Godsey et al., 2009):

$$q_1 = v_1 + w_1 \sin(\omega t + \varphi_1) \tag{4a}$$

$$q_2 = v_2 + w_2 \sin(\omega t + \varphi_2) \tag{4b}$$

$$f_1 = c_1(v_1 + w_1 \sin(\omega t + \varphi_1)) \tag{4c}$$

$$f_2 = c_2(v_2 + w_2 \sin(\omega t + \varphi_2)) \tag{4d}$$

with f_1 and f_2 the solute fluxes of the two tributaries. In order to reduce the number of model parameters that will need to be explored, we adopt the following normalization: $T = \omega t + \varphi_1$; $\phi = \varphi_2 - \varphi_1$; $Q_1 = \frac{q_1}{v_1}$; $Q_2 = \frac{q_2}{v_1}$; $F_1 = \frac{f_1}{v_1 c_1}$; $F_2 = \frac{f_2}{v_1 c_1}$; $W_1 = \frac{w_1}{v_1}$; $W_2 = \frac{w_2}{v_2}$; $r_Q = \frac{v_2}{v_1}$; and $r_C = \frac{c_2}{c_1}$. This yields:

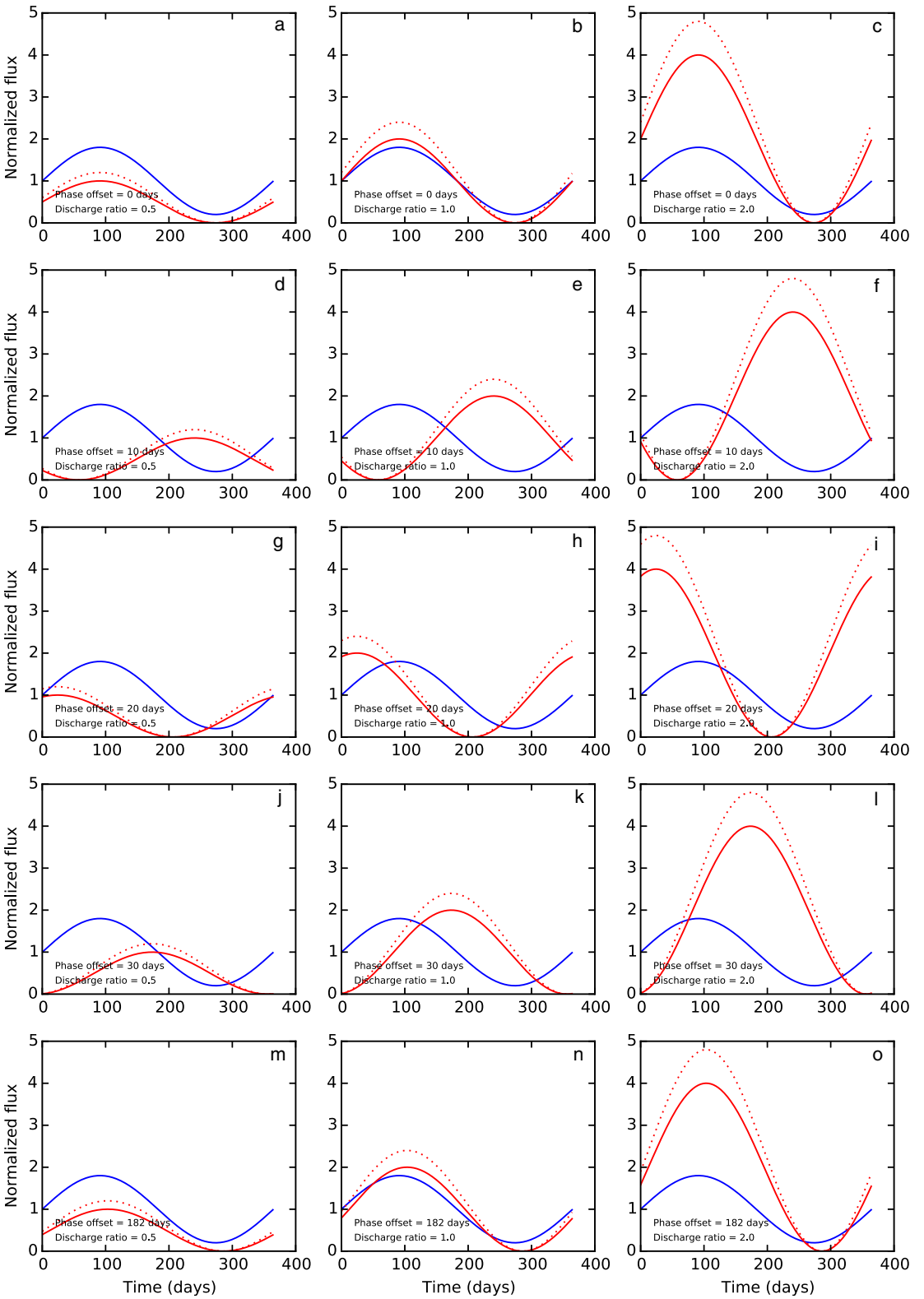

Figure 4. Synthetic time series of Q and F as inputs for the tributary mixing model. In this diagram concentration and discharge are normalized to the average of those of tributary *1*. The blue curve corresponds to the Q of and F of tributary *1* (the normalization scheme adopted here collapses these two time series on the same curve). The continuous red line corresponds to the Q of tributary *2*, and the dotted red curve to the F of tributary *2*. Each panel corresponds to a different combination of phase offset (ϕ in the text) between the two tributaries inputs, and to a different ratio of average Q between these two tributaries (r_Q in the text). The ratio of C between the two tributaries is maintained constant here ($r_C = 1.2$ see text).

$$Q_1 = 1 + W_1 \sin T \tag{5a}$$

$$Q_2 = r_Q(1 + W_2 \sin(T + \phi)) \tag{5b}$$

$$F_1 = 1 + W_1 \sin T \tag{5c}$$

$$F_2 = r_c r_Q(1 + W_2 \sin(T + \phi)) \tag{5d}$$

Here, Q and F are normalized to the time-averaged discharge and solute flux, respectively, of tributary *1*, and ϕ is the phase offset between the tributaries. W_1 and W_2 (positive and < 1) are the relative amplitude of variations of F and Q in each tributary. T is nondimensional and covers a whole period of variation between 0 and 2π.

We can now predict the evolution of C, Q and F in the mixture (C_m, Q_m, and F_m). Importantly, only Q and F (because we consider a conservative solute) can be summed, whereas the nonadditive property C_m has to be calculated by dividing F_m by Q_m:

$$Q_m = Q_1 + Q_2 = 1 + r_Q + W_1 \sin T + r_Q W_2 \sin(T + \phi) \tag{6a}$$

$$F_m = F_1 + F_2 = 1 + r_c r_Q + W_1 \sin T + r_c r_Q W_2 \sin(T + \phi) \tag{6b}$$

$$C_m = \frac{F_m}{Q_m} = \frac{1 + W_1 \sin(T) + r_c r_Q \left[1 + W_2 \sin(T + \phi)\right]}{1 + W_1 \sin(T) + r_Q \left[1 + W_2 \sin(T + \phi)\right]} \tag{6c}$$

From equations (6b) and (6c), C_m-Q_m relationships can be numerically predicted by varying T between 0 and 2π (a whole cycle of variation, corresponding, for example, to an annual cycle), for a range of values taken by the model parameters W_1, W_2, r_q, r_c, and ϕ. Different C_m-Q_m relationships are shown in Figure 5 for various values of the above-listed parameters. The corresponding inputs Q_1, Q_2, F_1, and F_2 are shown in Figure 4 and the resulting Q and F in the mixture (Q_m and F_m) are shown in supporting information Figure S40. Without phase offset between the tributaries ($\phi = 0$), no loop is observed (Figure 5, top), as the extrema in Q and F are reached simultaneously by the two tributaries. Depending on the values of r_c and r_q (and for a given value of $\frac{W_2}{W_1}$), the C_m-Q_m trend can be positive or negative (see also supporting informationsection S3 for an algebraic proof of this observation). Conversely, phase offset between the two tributaries generates hysteresis in the C_m-Q_m relationship. Increasing the concentration ratio r_c between the two tributaries makes the loop "deeper" (i.e., more extended in the vertical direction), while increasing the ratio of average discharge, $\frac{w_2}{w_1}$, "widens" this loop (i.e., makes it larger in the horizontal direction). This is because the range of Q (respectively C) that can be reached by the mixture is higher if the two tributaries have drastically different Q (respectively C) - as long as they are not in phase opposition. Altogether, this numerical experiment shows that a range of very diverse C-Q relationships, both in trend and shape, can be obtained simply by mixing a conservative solute from two tributaries displaying sine-wave variations in this solute's flux.

4.2. First-Order Predictions in the Context of the Amazon Basin

Regarding the trend (b-value) of the C-Q relationship in the modeled mixture, we can predict, for different sets of parameters, the sign taken by the derivative of C_m with respect to Q_m as a function of T, which in turn indicates the slope in the C_m-Q_m diagram. In the supporting information section S3, we provide this derivation, and show that the parameters that will drive the sign of $\frac{dF_m}{dQ_m}$ are r_c, r_q, ϕ, and $\frac{W_2}{W_1}$ or $\frac{w_2}{w_1}$. The first parameter r_c is related to the difference between the two tributaries in terms of chemical composition, while the others are related to the hydrological pattern of Q time series. Specifically, a change in the b-exponent after mixing is predicted to happen by our model as long as the tributaries differ in C ($r_c \neq 1$), as shown in Figure 5. In particular, a decrease in the b-value will occur through mixing if the tributary with the highest C is the one exhibiting the smallest variations in Q (see supporting information section S3). In the context of the Amazon Basin, Tables 2 and 3 show that in general, northern Andean stations have higher mean C than their "pure Lowland" counterparts (e.g., FOR-BOR-ATA versus LAB-SER-CAI-ITA). Although the case of the southern region of the Amazon Basin cannot be examined directly with the data presented in Table 2, we can predict that downstream stations, where solute-rich, Andean-derived waters are admixed to more dilute lowland waters, should display lower b-values and therefore more dilutional patterns.

This first-order prediction on the downstream evolution of b-values can be refined for each solute, considering their main pathways of production in the Amazon basin, for which a wealth of background information

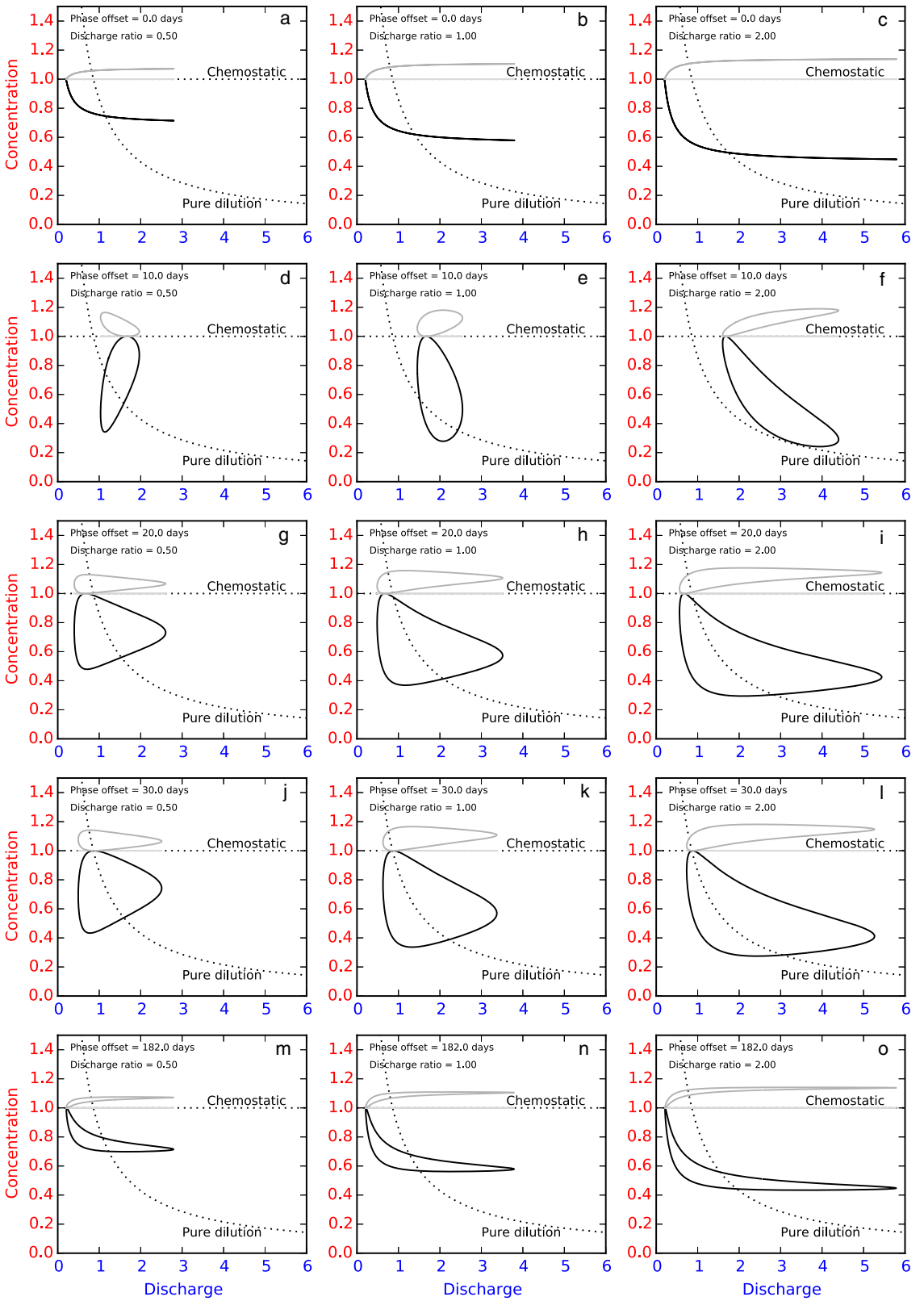

Figure 5. Result of the tributary mixing model in terms of *C-Q* relationships. In this diagram *C* and *Q* are normalized to the average of those of tributary *1*. In each panel, each curve represents a different value of the ratio of *C* between the two tributaries (defined as r_C in the text; black line: 0.2; horizontal grey line: 1.0, thin grey line: 1.2). The trends of the "chemostatic" and dilutional behaviors are indicated for comparison (the exact vertical position of these trends are arbitrary). Each panel then corresponds to a different combination of phase offset (ϕ in the text) between the two tributaries inputs, and to a different ratio of average *Q* (r_Q in the text) between the two tributaries.

exists. The strongest decrease of the *b*-exponent should be observed for solutes exhibiting the largest difference in *C* between the Andean-derived waters and the waters derived from low-relief areas. This is the case for Na^+, Cl^- and SO_4^{2-}, which are dilute in low-relief rivers (Moquet et al., 2016). The main source of these species in the low-relief area of the Amazon is the atmosphere, because silicate weathering (which could release Na^+) is slow there, and because evaporite and sulfide dissolution (which could release Na^+, SO_4^{2-}, or Cl^-) are virtually absent (Moquet et al., 2011; Torres et al., 2015). On the other hand, for solutes which are significantly present in "pure low-relief" waters ($r_c \sim 1$), we predict a smaller change of the *b*-value of *C*-*Q* relationships in the mixture, such that the *C*-*Q* behavior of these solutes should remain closer to being "chemostatic" throughout the basin. This should be the case for Si and K^+, as indicated by the *C* data (Table 3) and by pluri-annual budgets showing the significant inputs of these two solutes in lowland regions (Moquet et al., 2016). It is worth noting that these two elements are important nutrients, and that therefore their behavior might be influenced by vegetation and/or plankton development in the highly productive lowland regions (Fraysse et al., 2006; Konhauser et al., 1992; Lucas, 2001; Moulton et al., 2000). Moreover, thermodynamical equilibrium between solution and secondary silicate minerals could also control the fluxes of these two particular elements and set their concentration to nearly constant values (e.g., Clymans et al., 2013; Hughes et al., 2013; Neal et al., 2005).

None of the models recently developed to examine *C*-*Q* relationships (e.g., the "PPA model" of Godsey et al., 2009, or the 1D-reactive transport model of Maher, 2011) can account for *C*-*Q* hysteresis loops. However, Moquet et al. (2016) showed that for the Amazon at Óbidos such hysteresis loops could be reproduced by summing the monthly inputs of the different tributaries. Hysteresis is thus most likely an important feature of *C*-*Q* relationships when tributary mixing needs to be evaluated. Therefore, and aside from the downstream change in the *b*-exponent of *C*-*Q* relationships, following the numerical experiments of section 4.1, *C*-*Q* hysteresis loops occur in the mixture only if there is a phase shift ($\phi \neq 0$) between the tributaries (Figure 5). This condition is clearly met in the Amazon as the precipitation and discharge patterns vary greatly between (1) Andean and Lowland regions due to orographic effects (Espinoza et al., 2015); (2) different and large subbasins (e.g., Negro, Solimões, and Madeira rivers) due to the migration of the SAMS spatial and variability in intensity during the year (Espinoza et al., 2009b; Guimberteau et al., 2012; Vera et al., 2006) (Figure 1). Given this hydroclimatic spatial variability across the Amazon Basin in terms of timing of peak discharges in the year (Figure 1c) and *Q* variability (Table 2), we can expect that the largest subbasins, integrating over vast areas of the Amazon Basin, will display wider hysteresis loops.

To summarize, our model leads us to expect that, in the context of the Amazon Basin, *C*-*Q* relationships should become more "dilutional" downstream through mixing of compositionally different tributaries, especially through the admixture of relatively dilute, "pure" Lowland waters to more solute-rich, Andean-derived waters. This effect should be more prominent for solutes for which the Andean region is the main source, i.e., Na^+, Cl^- and SO_4^{2-}, whereas for solutes significantly produced in the Lowlands such as K^+ and Si, the *C*-*Q* relationships should remain relatively "chemostatic." Additionally, the *C*-*Q* relationships should also exhibit wider hysteresis loops downstream. In the following section we test these predictions against observations summarized in our database.

5. Comparison With Field Data

5.1. Validity of the Assumptions Underlying the Model

Before checking our model predictions against real-world data, it is necessary to evaluate the validity of the assumptions underlying the model in the context of the Amazon Basin, the natural laboratory chosen for the present study. Basically, our mixing model represents what we can call from a conceptual point of view a "case of aggregation." More physically, this corresponds to a confluence or a set of confluences, plus the river reaches (including associated floodplains) between the different upstream and downstream stations of observation. At the time resolution used in this study, two main assumptions are thus underlying our mixing model. First, the solutes under consideration need to be conservative during water mixing (such that at all times $F_1 + F_2 = F_m$). Second, any signal smearing and phase shifting, by the effect of transport alone (Kirchner, 2016a), should be negligible. In a more operational phrasing, this latter condition is equivalent to saying that the upstream and downstream stations of measurements are sufficiently close to one another such that any effect of transport between these stations (in the river reach and associated floodplains) can be neglected.

We first note that the requirement of solute conservativity is most likely fulfilled by the major solutes under consideration here, as shown by the systematic studies of the "Encontro das Aguas" mixing zone at the confluence between the Solimões and Negro rivers (e.g., Aucour et al., 2003; Guinoiseau et al., 2016; Laraque et al., 2009). The validity of the second assumption can be evaluated by comparing the properties (mean, amplitude of variation, phase) of signals (discharge and solute fluxes) upstream and downstream from real-world cases of aggregation. However, this requires in turn that all the input fluxes upstream of the case of aggregation are known, in order to obtain a reliable estimate of the summed input flux. We emphasize that such approach is possible only for additive properties such as discharge and solute fluxes - provided, again, that these solutes are conservative during mixing - and not for solute concentration, hence the interest of considering Q and F in the present analysis. In the supporting information section S4 and Table S2, the effect of transport on the signals of discharge and solute fluxes is evaluated in detail for two cases of aggregation in the Amazon for which all input fluxes are known, namely PVE $\rightarrow$ FAZ and MAN + SER + CAI + FAZ $\rightarrow$ OBI. Our analysis shows that even over the relatively long river reaches characterizing these two cases of aggregation, and despite the presence of significant water and solute routing through floodplains, the signals are not significantly affected by transport, at least at the time resolution (10 day period) of the present study.

To summarize, the two main assumptions underlying our tributary mixing model presented in section 4 are shown to be broadly valid in the case of the Amazon Basin.

5.2. Concentration-Discharge Relationships in the Amazon

5.2.1. Trends: b-Values

In the Amazon, major solute *C-Q* relationships are very diverse in shape (Figure 6 and supporting information Figures S47-S59). We fitted the two parameters of $\log C = a + b.\log Q$ to the 10 day period C and Q time series using the Python Numpy *polyfit* function, to obtain the parameters of equation (3). Most *C-Q* relationships can be reasonably fitted with by a power law with a 0-to-negative b exponent, as observed by Godsey et al. (2009) for small basins, Moon et al. (2014) for large rivers, or Torres et al. (2015) and Moquet et al. (2016) for rivers of the Amazon system. Concentration-discharge relationships in the Amazon thus cover the full range of behavior between "pure dilution" (best represented by Cl^- at OBI with a b-value of -1.06 ± 0.04; Figures 6 and 7) and "chemostatic" (with b-values undistinguishable from 0: Si at BOR, LAB, PVE and FAZ; Na^+ at SER and ITA; K^+ at ATA, SER, and TAB; Mg^{2+} at BOR and CAI; Ca^{2+} at BOR, SER, and CAI; and SO_4^{2-} at BOR and ITA). For some stations/solutes C even increases with Q (significantly positive b-values): Si at TAB; K^+ at BOR, RUR, ITA, and PVE; Mg^{2+} at SER; Ca^{2+} at ITA; Cl^- at SER. The most consistent trends are usually obtained for solutes showing a strong dilution effect (such as Cl^- at OBI; Figure 6), while a large relative dispersion exists for elements with a flatter pattern in the *C-Q* diagrams (such as K^+ at ATA; Figure 6).

The largest b-values (in absolute value; Table 4 and Figure 7) are obtained for Cl^- (mean of -0.40 [from -1.06 to 0.22]) and Na^+ (-0.31 [-0.82 to 0.02]) while Si and K^+ display the values closest to 0 (-0.07 [-0.33 to 0.07] and -0.04 [-0.49 to 0.10], respectively). Andean stations usually exhibit b-values closer to 0 (e.g., from -0.04 to -0.32 depending on the solute for FOR) compared to downstream stations (-1.06 to -0.33 for OBI). Therefore, in general lower b-values are observed for mixed rivers compared to rivers draining only the Andes or the Lowlands (Figure 7). The effect is stronger for Na^+ and SO_4^{2-} than for Ca^{2+} and Mg^{2+}. Chlorine displays the lowest b-values of all elements for most basins, but has higher b-values in basins draining exclusively the low-relief areas (stations LAB, SER, CAI, ITA). Finally, there is almost no difference in the b-value of Si and K^+ across the different river types, with values mostly around 0 ("chemostatic"), except for the largest basins (stations MAN and OBI).

These observations, confirming and refining those of Torres et al. (2015) and Moquet et al. (2016) on the downstream evolution of b-exponents across geomorphic gradients, are therefore entirely compatible with the predictions based on our tributary mixing model developed in section 4.

5.2.2. Shape: C-Q Hysteresis Loops Quantified by Phase Offset Between Discharge and Solute Fluxes

Concentration-discharge relationships are parametric curves where time is the implicit parameter, and where two signals (C and Q) are plotted against each other. In such a diagram, loops will appear if there is a difference in time between the peaks of the two signals. If the two signals vary with no offset between their peaks, a positive trend, without any loop is obtained (panels a to c in Figures 4 and 5). Similarly, if the two signals vary in phase opposition, a negative trend, without any loop is obtained a situation close to that

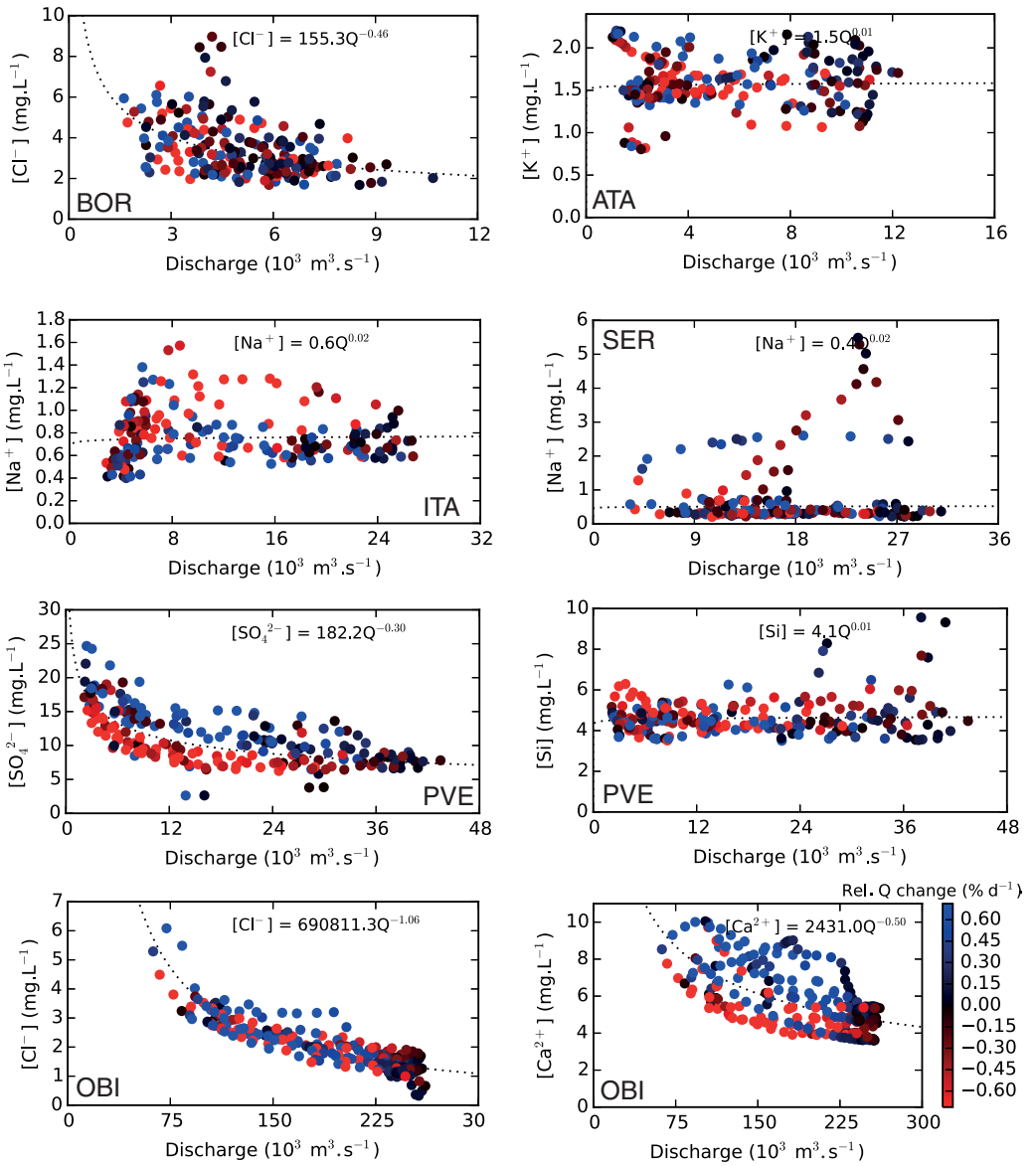

Figure 6. Concentration-discharge (*C-Q*) relationships for a selection of gauging stations and solutes. The power law best fit is indicated as a dotted curve, along with the best fit equation (where concentrations in bracket are in mg.L^{-1} and *Q* is in m^3.s^{-1}). The exponent of this equation is the *b*-exponent of the *C-Q* relationship. In such diagrams, a strictly chemostatic behavior corresponds to a horizontal line. The data points are color-coded following the instantaneous relative *Q* change, calculated as the derivative of *Q* with respect to time, divided by the value of *Q*, and expressed in %. Negative values (red dots) correspond consequently to decreasing discharge while positive values (blue dots) correspond to increasing discharge. In order to optimize the use of the colorbar, the colorbar limits were set to + and - the standard deviation of the relative *Q* change recorded at the station. Here the exact values along the colorbar refer only to the Óbidos station (OBI).

depicted in (panels m to o in Figures 4 and 5). On the contrary, any offset between the peaks will make the two signals attain their extrema at different times, thereby generating hysteresis in the parametric curve (panels d to l in Figures 4 and 5). In the present study we use the phase offset between the signals of discharge and solute fluxes of a given river as a metric for the significance of *C-Q* hysteresis loops. The validity of this metric is demonstrated in the supporting information section S5.

The phase offset between *F* and *Q*, $\varphi_F - \varphi_Q$, is provided in Table 5 and displayed in Figure 8. For most solutes, *F* peaks lag behind *Q* peaks (significantly positive values of $\varphi_F - \varphi_Q$) at the Andean station BOR and at

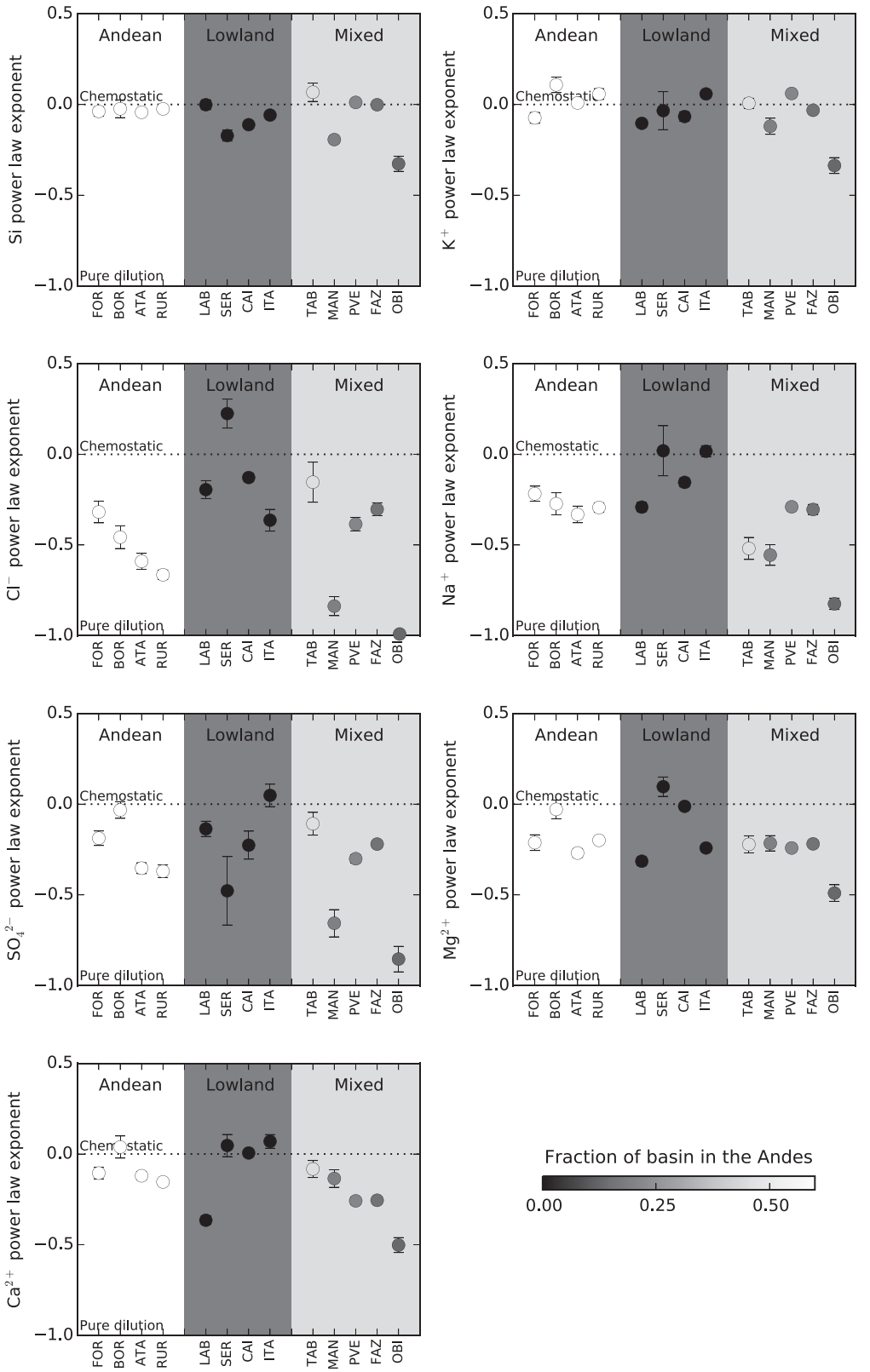

Figure 7. *b*-exponent power law best fits of *C*-*Q* relationships (e.g., Figure 6) for the different domains of the Amazon Basin, as defined in Figure 1b. A value of 0 corresponds to a chemostatic behavior (meaning that *C* is constant despite *Q* variations); a value of −1 indicates a pure dilutional behavior. Data points are color-coded following the proportion of the corresponding drainage area that is located in the Andes. The *b*-values are reported in Table 4.

Table 4
"b-exponent" Power Law Best Fits of C-Q Relationships for Each Solute and Station

	Si		SO_4^{2-}		Cl^-		Na^+		K^+		Mg^{2+}		Ca^{2+}	
	Mean	1 s.d.	Mean	1 s.d.	Mean	1 s.d.	Mean	1 s.d.	Mean	1 s.d.	Mean	1 s.d.	Mean	1 s.d.
FOR	−0.04	0.03	−0.19	0.04	−0.32	0.06	−0.22	0.04	−0.07	0.03	−0.21	0.03	−0.11	0.04
BOR	−0.02	0.05	−0.03	0.05	−0.46	0.06	−0.27	0.06	0.11	0.04	−0.03	0.06	0.04	0.05
ATA	−0.04	0.02	−0.35	0.03	−0.59	0.04	−0.33	0.05	0.01	0.02	−0.27	0.02	−0.12	0.02
RUR	−0.02	0.01	−0.37	0.04	−0.66	0.03	−0.29	0.02	0.06	0.03	−0.20	0.02	−0.15	0.02
LAB	0.00	0.03	−0.14	0.04	−0.19	0.05	−0.29	0.03	−0.10	0.02	−0.31	0.02	−0.37	0.02
SER	−0.17	0.03	−0.48	0.19	0.22	0.08	0.02	0.14	−0.03	0.11	0.10	0.06	0.05	0.05
CAI	−0.11	0.01	−0.23	0.08	−0.13	0.02	−0.15	0.02	−0.07	0.03	−0.01	0.02	0.01	0.02
ITA	−0.06	0.01	0.05	0.06	−0.36	0.06	0.02	0.03	0.06	0.02	−0.24	0.04	0.07	0.02
TAB	0.07	0.05	−0.11	0.06	−0.15	0.11	−0.52	0.06	0.01	0.03	−0.22	0.05	−0.08	0.05
MAN	−0.19	0.02	−0.66	0.08	−0.84	0.05	−0.56	0.06	−0.12	0.04	−0.22	0.05	−0.14	0.04
PVE	0.01	0.01	−0.30	0.02	−0.38	0.04	−0.29	0.02	0.06	0.01	−0.24	0.02	−0.26	0.02
FAZ	0.00	0.01	−0.22	0.02	−0.30	0.04	−0.30	0.03	−0.03	0.02	−0.22	0.02	−0.26	0.02
OBI	−0.33	0.04	−0.85	0.07	−1.06	0.04	−0.82	0.03	−0.34	0.04	−0.49	0.04	−0.50	0.05

the downstream stations MAN, PVE, FAZ, and OBI. For the lowland station ITA, most *F* peaks occur earlier in the year than the *Q* peak. For most solutes, uncertainties preclude the measurement of any phase offset between *F* and *Q* peaks for stations FOR, SER, and CAI, In terms of absolute value, the phase offset $|\varphi_F - \varphi_Q|$ of most solutes is in the range 0 (meaning that *Q* and *F* vary at pace) to 23 days for Si at TAB and to 89 days for SO_4^{2-} at OBI. For a given solute, there are significant differences in phase offset between stations (Table 5). Although phase offset remains in a relatively limited range across the set of stations for Cl^-, Na^+, and Si, for the other solutes $\varphi_F - \varphi_Q$ is higher in mixed rivers than in rivers draining only the Andes or the Lowlands (Figure 8), indicating that hysteresis loops are more prominent at downstream stations than at upstream ones. The fact that hysteresis loops are wider at downstream stations is expected from our modeling results, as these stations collect water from a range of areas spanning different hydroclimatic regimes, and therefore are the most likely to have tributaries which differ in timing of peak discharge and amplitude of variations. On average the lowest mean $|\varphi_F - \varphi_Q|$ are those of Si, Na^+, K^+, and Cl^-, whereas the *F* peaks of Mg^{2+}, Ca^{2+}, and SO_4^{2-} fluxes have longer time lags with *Q* peaks. This pattern is consistent with the fact that Si

Table 5
Phase Offset Between Q and F (as a Measure of Hysteresis in C-Q Relationships) for Each Solute and Station

	Si		SO_4^{2-}		Cl^-		Na^+		K^+		Mg^{2+}		Ca^{2+}	
	Mean	1 s.d.	Mean	1 s.d.	Mean	1 s.d.	Mean	1 s.d.	Mean	1 s.d.	Mean	1 s.d.	Mean	1 s.d.
	days		days		days		days		days		days		days	
FOR	17	12	12	43	−55	500	24	62	−6	54	22	13	8	101
BOR	4	3	35	2	−28	68	−9	8	16	13	25	1	36	7
ATA	−2	1	−5	0	−19	2	−1	2	4	2	−3	0	4	1
RUR	−5	4	4	2	11	41	1	6	−1	18	−1	2	−2	5
LAB	10	1	18	4	3	50	−3	3	8	5	−5	1	−3	5
SER	2	2	−81	172	11	34	−9	8	9	13	−1	11	14	28
CAI	−2	3	11	67	14	33	−2	8	10	15	−1	12	0	23
ITA	−6	0	−4	30	−3	11	−14	4	−4	2	−12	2	−16	3
TAB	−23	0	−6	0	−25	1	33	0	−2	1	15	0	20	1
MAN	1	0	78	0	3	1	−4	0	25	1	29	0	34	0
PVE	−4	0	18	0	−11	4	−3	1	2	1	2	0	9	1
FAZ	4	0	11	0	10	2	11	1	6	1	8	0	12	0
OBI	3	0	89	0	128	2	20	0	35	0	51	0	44	0

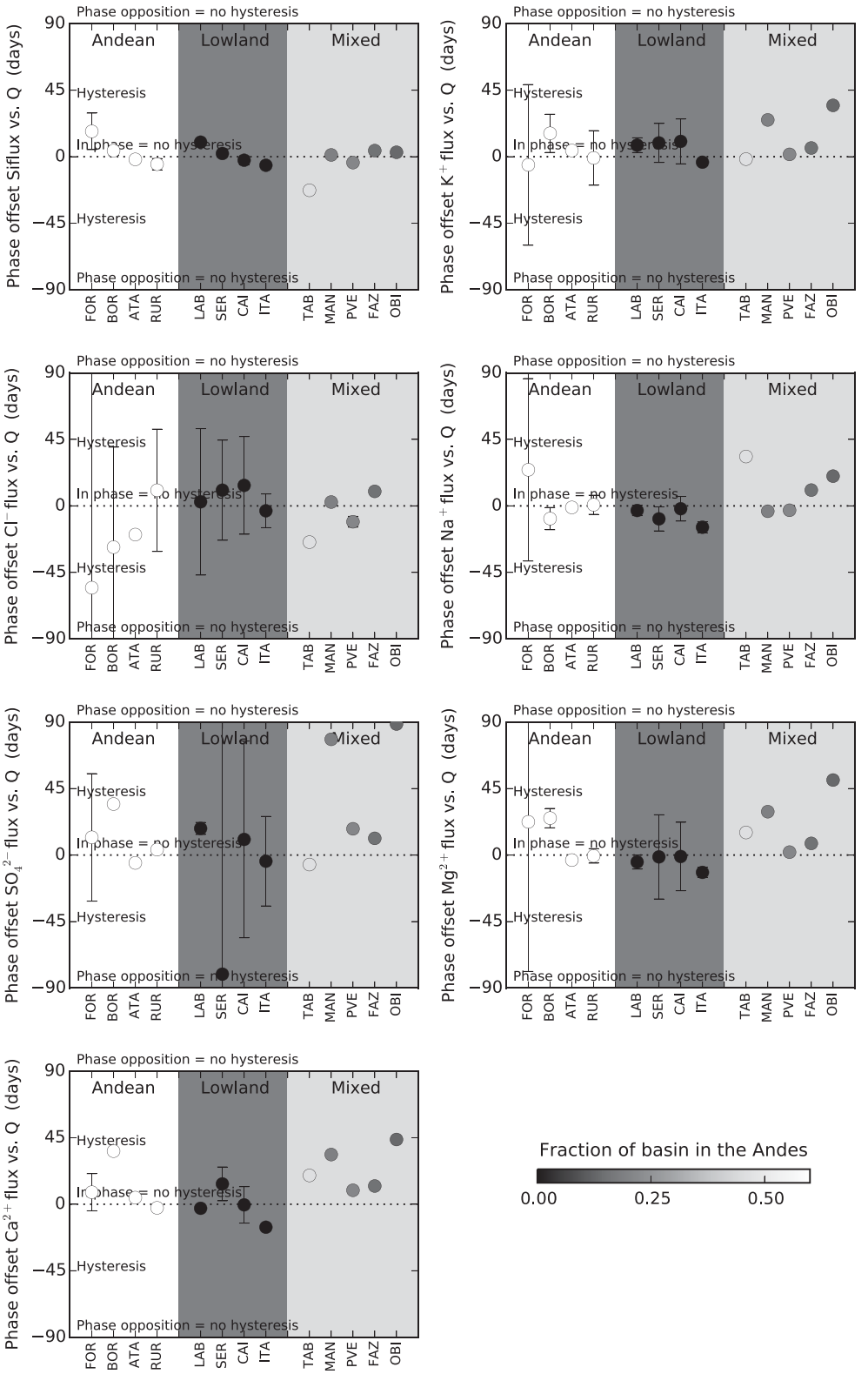

Figure 8. Phase offset between *Q* and *F* (as a measure of hysteresis in *C-Q* relationships) for the different domains of the Amazon Basin, as defined in Figure 1b (see supporting information section S5 and supporting information Figures. S45 and S46). A value of 0 days indicates that variation in *Q* and *F* are in phase, and values of 182 or −182 days (half a year) correspond to the case where *Q* and *F* are in phase opposition. Between these values, phase offset indicate the presence of hysteresis in *C-Q* relationships. Data points are color-coded following the proportion of the corresponding drainage area that is located in the Andes. The data used in this figure are reported in Table 5.

and K^+ display a relatively homogenous concentration across the Amazon Basin regardless of the domain (Table 3). In such conditions of homogenous concentration (i.e., $r_c \sim 1$), our model predicts chemostatic *C-Q* relationships in the mixed waters regardless of the phase offset between the tributaries input (supporting information section S3), meaning in turn that *F* and *Q* vary in phase in these mixed waters.

To our knowledge this is the first time that a systematic trend in the magnitude of *C-Q* hysteresis loops versus catchment heterogeneity is reported. This trend is compatible with the predictions based on our tributary mixing model presented in section 4.

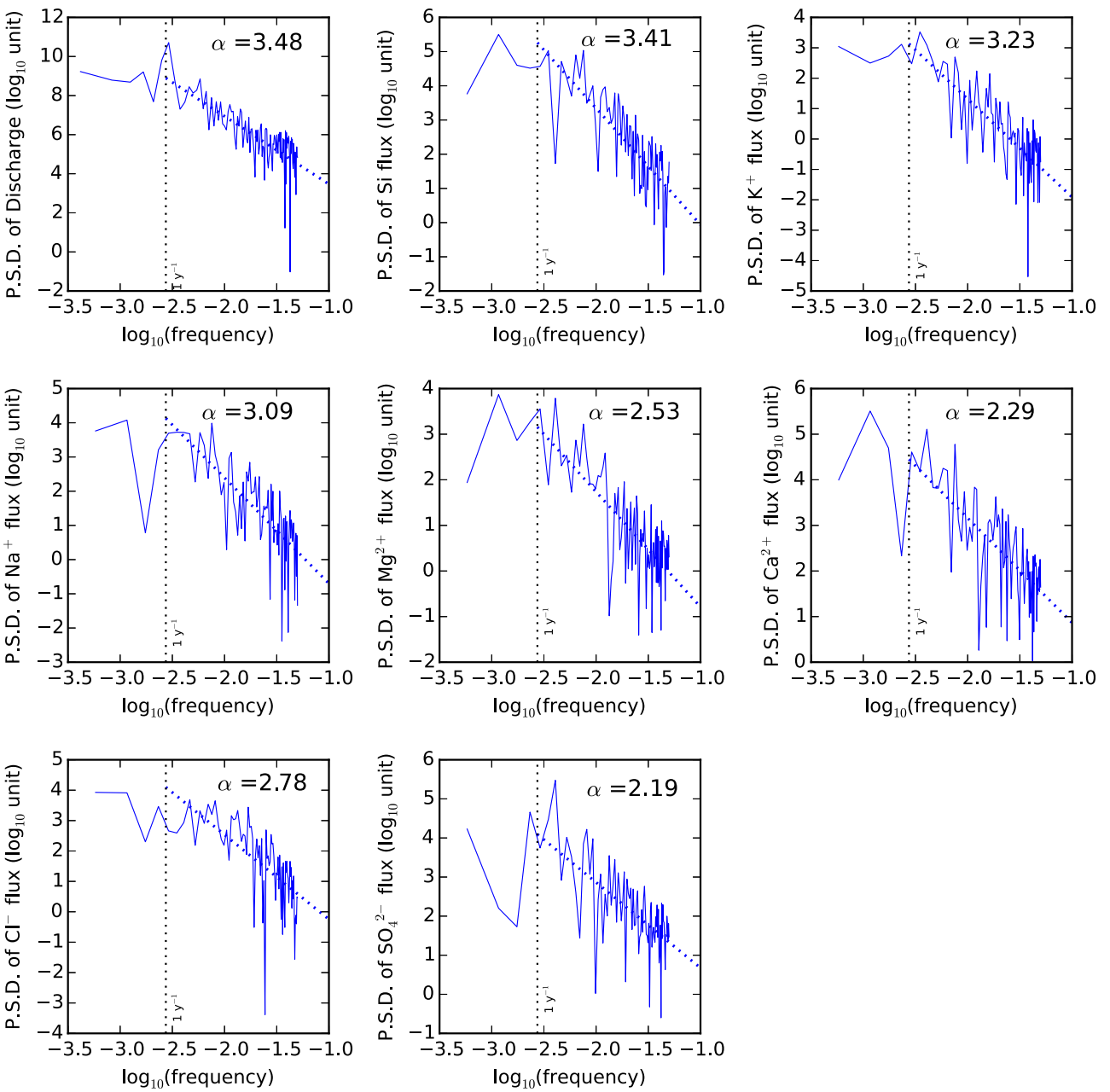

Figure 9. Power spectral density (P.S.D) of discharge (*Q*) and solute fluxes (*F*) for the station OBI (at the mouth of the Amazon) for the 7 major solutes considered in this study (see supporting information section S1). The frequency of 1 y^{-1} is indicated as a vertical dotted line. The other dotted line is the power law best fit (linear in this log-log plot) of the power density spectrum for frequencies above 1 y^{-1}, and the scaling factor α (exponent of this power law best fit) is provided in each panels.

5.3. Discussion and Implications

To summarize, our analysis shows that the *C*, *Q*, and *F* time series of 13 gauging stations of the SNO-HYBAM network on the Amazon are fully compatible with our model of tributary mixing. In addition, the shifts in the trend and shape of *C*-*Q* relationships are accounted for by our mixing model, for all solutes considered. Obviously, alternative models can reproduce the data, but in any case tributary mixing does occur in large river systems and therefore has to be taken into account. We also acknowledge that other factors and processes are at play when comparing different stations across the Amazon basin. Solutes can be reactive such that they are not only added downstream but can be lost, for example, by adsorption or mineral precipitation or vegetation uptake e.g., in floodplains or alluvial deposits (Bouchez et al., 2012) or at confluences (Guinoiseau et al., 2016). Although the list of elements selected for the present study most likely fulfill this condition of solute conservativity, additional complexities (e.g., water and solute routing through floodplains) might affect the exact figures presented in this study. However, despite these additional complexities that cannot be taken into account for now, both by lack of data and difficulty of building up a simple tractable model, the first-order analysis performed here supports a control of large-scale *C*-*Q* relationships by mixing.

Hydrochemical time series often display variations at all time scales. Spectral analysis is therefore a powerful approach to examine the behavior of these different frequencies contributing to the signal, and to explore how the signal is modified by a given operator (e.g., a catchment or a river reach) as a function of frequency (Aubert et al., 2013; Duffy & Gelhar, 1985, 1986; Godsey et al., 2010; Kirchner & Neal, 2013; Kirchner et al., 2000, 2001; Neal et al., 2012). We computed the Fourier transform of the *Q* and *F* time series (see supporting information section S1). Hydrochemical time series of relatively small systems have been reported to universally follow a "$1/f$" scaling, i.e., their power spectral density varies as a function of $1/f^{-\alpha}$ (with $\alpha > 0$) for frequency higher than some threshold. This approach was hitherto applied to *Q* and *C* time series, but here we expand its use to *F* time series (see supporting information section S1). A large value of α means in particular that the contribution of high frequencies is much smaller than that of low frequencies. Therefore we use α as a measure of the dominance of the 1 y^{-1}-frequency over higher frequencies in the *Q* and *F* time series. The power spectral density of *Q* and *F* are shown in Figure 9 and supporting information Figures S1–S13. All spectra show the highest power for the 1 y^{-1}-frequency, with a strong decrease of the power for higher frequencies. The spectra can be reasonably fitted by a power law for frequencies higher than 1 y^{-1}, yielding the α-value. The *Q* α -values (Table 6) vary from 1.25 (CAI) to 3.48 (OBI), and span a wider ranger than that reported for smaller basins by Kirchner et al. (2000, 2001), Godsey et al. (2010), Neal et al. (2012), Kirchner and Neal (2013), or Aubert et al. (2013) with most values in the range 1–2. Values of α for *F* are commensurate to those of *Q*, consistent with the fact that the variations of *C* are relatively small and that at first order, *F* scales with *Q* across the set of gauging stations and solutes considered. Fluxes α values range from 0.01 (Si at FOR, a value equivalent to white noise, i.e., same power of all frequencies) to 4.28 (Cl^- at

Table 6
"1/f-Scaling Factor" α of Power Density Spectra (e.g., Figure 9) of Discharge (Q) and Solute Fluxes (F)

	Discharge		Si		SO_4^{2-}		Cl^-		Na^+		K^+		Mg^{2+}		Ca^{2+}	
	Mean	1 s.d.	Mean	1 s.d.	Mean	1 s.d.	Mean	1 s.d.	Mean	1 s.d.	Mean	1 s.d.	Mean	1 s.d.	Mean	1 s.d.
FOR	0.7	0.3	0	0.3	0.6	0.3	1.2	0.3	0.5	0.3	0.5	0.3	0.1	0.2	0.5	0.3
BOR	1.4	0.4	1.5	0.3	1.5	0.3	1.1	0.3	0.9	0.3	1.8	0.4	1.8	0.3	1.9	0.3
ATA	1.5	0.3	2	0.3	2.1	0.3	2.3	0.3	2.4	0.3	1.9	0.3	2.1	0.4	2	0.3
RUR	1.4	0.3	1.7	0.3	1.6	0.3	1.5	0.3	1.8	0.3	1.8	0.3	1.5	0.3	1.4	0.3
LAB	2.1	0.3	1.3	0.2	2	0.4	2.9	0.4	2.8	0.3	2.4	0.3	2.5	0.4	2.5	0.4
SER	2.9	0.3	2.3	0.3	2.9	0.4	3.1	0.3	3.4	0.3	2.6	0.4	2.3	0.4	2.4	0.3
CAI	1.3	0.3	1.7	0.3	2.5	0.3	2.6	0.3	2.1	0.3	1.9	0.4	1.8	0.4	1.6	0.4
ITA	2.5	0.3	1.8	0.4	3.5	0.4	3	0.4	2.7	0.4	2.4	0.4	1.9	0.3	3.1	0.4
TAB	2.3	0.3	4	0.3	2.6	0.3	2.6	0.4	3	0.3	2.1	0.3	2.7	0.3	1.7	0.3
MAN	3.2	0.3	1.8	0.3	2.8	0.4	3.5	0.3	2.8	0.4	2.7	0.3	2	0.3	2	0.3
PVE	2	0.3	2.9	0.3	2.4	0.4	4.3	0.4	3	0.4	3	0.3	2.2	0.3	2.8	0.3
FAZ	2.1	0.3	2.7	0.3	3	0.3	2.9	0.3	3	0.3	3.4	0.3	3.1	0.4	3.5	0.4
OBI	3.5	0.3	3.4	0.3	2.2	0.3	2.8	0.4	3.1	0.3	3.2	0.3	2.5	0.3	2.3	0.3

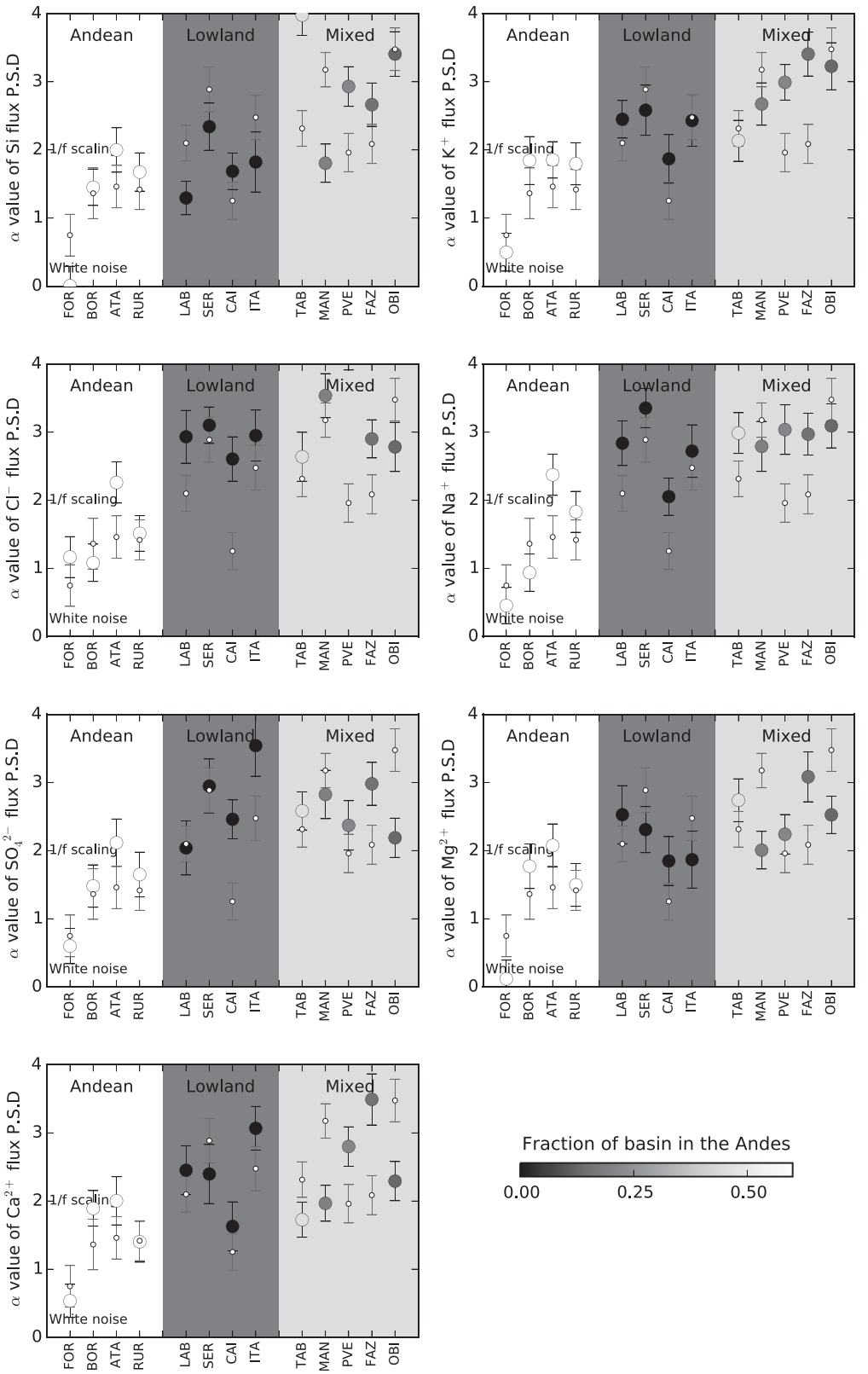

Figure 10. "1/f-scaling factor" α of power spectral density (e.g., Figure 9) of discharge (small open circles) and solute fluxes (large colored circles) for the different domains of the Amazon Basin, as defined in Figure 1b. A value of 0 corresponds to "white noise" (meaning that all frequencies contribute equally to the signal); higher values indicate 1/f-scaling. Data points are color-coded following the proportion of the corresponding drainage area that is located in the Andes. The α-values are reported in Table 6.

PVE), but no systematic difference is observed between two given elements. However, there is a clear difference in α values between the different river types: from 0.01 (Si at FOR) to 2.37 (Na^+ at ATA) for Andean stations; from 1.29 (Si at LAB) to 3.54 (SO_4^{2-} at ITA) for pure Lowland rivers; and from 1.80 (Si at MAN) to 4.28 (Cl^- at PVE) for the most downstream stations (Figure 10). To our knowledge, this is the first time that such a spectral analysis of solute river fluxes is conducted, especially at this large scale, and the first time that a change in the scaling factor of power spectral spectra of hydrochemical fluxes, as a function of basin heterogeneity is reported. A preliminary analysis suggests that this change in the α-value of *F* and *Q* time series across our set of gauging stations (Figure 10) is not due to transport of water and solutes alone (see supporting information section S4). One alternative explanation would be that mixing leads to this continental-scale dampening of high-frequency signals. This would be possible if the high-frequency components of the various inputs were likely to cancel out (e.g., were in phase opposition), which is plausible but remains to be tested with a more systematic assessment of the phase lags of *Q* and *F* between different regions.

The present case study focuses on the sole Amazon Basin, but we suggest that our findings should be applicable to other large river basins. Indeed, the world's largest river basins also drain areas with contrasted characteristics in terms of landscape, lithology, climate, and ecosystems. However, we also emphasize that for a particular system, other factors might have to be taken into account and the model might require some adjustments. For example, the downstream evaporative loss that occurs in semiarid systems will exert an additional influence on solute concentration and more generally *C-Q* relationships at the most downstream stations.

We show that mixing of water and solutes between compositionally different tributaries produces downstream shifts in *C-Q* relationships, both in terms of trends (*b*-exponent) and shape (hysteresis). This fact challenges the use of *C-Q* relationships to infer weathering properties in large catchments, where aggregation of such heterogeneity is most likely. This whole view could be "downscaled" to a smaller, more homogenous catchment. Indeed, even in small catchments, packets of water follow different flowpaths acquire different chemical composition and mix before or when entering the stream where the gauging station is located. One prominent example of such flowpath distribution would be the separation between "surface runoff" and deeper groundwater (e.g., Calmels et al., 2011). The relative contribution of these different flowpaths will vary through time depending on hydroclimatic conditions, just like for tributaries in a large river basin, as shown by hysteresis loops in *C-Q* relationships of small basins recorded during storm events. Therefore, characteristics of *C-Q* relationships, even in small catchments, could also simply result from mixing of different flowpaths. To circumvent such issues one possibility could be to select solutes such that they reflect the input of only one of the water reservoirs.

6. Conclusion

In this paper we addressed the downstream evolution of concentration-discharge (*C-Q*) relationships in large systems, using the Amazon basin in a case study. In such large systems, as water and solutes move downstream they mix with water and solutes from compositionally different tributaries. Therefore, we explored how mixing between these different types of water could affect *C-Q* relationships and potentially hamper their use as messengers of the Critical Zone in terms of weathering properties. Based on discharge and solute concentration at a 10 day frequency recorded across 13 gauging stations throughout the Amazon basin, we show the following downstream evolution:

- Increase in the exponent ("*b*") of power law best fit of *C-Q* relationships, from a quasi "chemostatic" (constant *C*) behavior in homogenous basins (i.e., those draining only the lowlands, or only the Andes) to more dilutional behavior in more heterogeneous basins.
- Increase in the magnitude of *C-Q* hysteresis loops, especially for the most downstream stations, due to an increase in the phase offset between discharge and solute flux signals of the different tributaries.

We built up a simple model of tributary mixing, which predicts, given the differences in water and solutes input signals between tributaries draining different geomorphic/hydroclimatic subregions in the Amazon, the above patterns. These findings have broader implications for *C-Q* relationships in other large river systems, but also for smaller systems where mixing of different flowpaths could lead to the same effects on the *C-Q* relationships.

From the methodological perspective, we also showed that *C-Q* hysteresis is an overlooked feature of *C-Q* relationships that can be highly informative to detect mixing or more generally to discriminate between different models aiming at reproducing *C-Q* trends. We suggest that the phase offset between *Q* and *C* (or flux time series *F*) could be used as a simple proxy for quantification of *C-Q* hysteresis loops. Finally, we show how solute fluxes *F*, as additive properties like *Q* but unlike *C*, can be used in tributary mixing models and in spectral analysis to retrieve transport properties - but also potentially reactivity - of chemical elements in the Critical Zone.

Acknowledgments
Additional information is available in the supporting information of this manuscript. Original data can be found at on the SNO-HYBAM website (http://www.ore-hybam.org). We are grateful to J. West, M. Torres, J. Baronas, J. Gaillardet, P. Floury, and the whole HYBAM team for fruitful scientific discussions. M. Albenque is thanked for checking the mathematical derivations. Data used in this study can be dowloaded from http://www.ore-hybam.org/. This work was partially funded by the Programme "Émergences" of the City of Paris "Chemical weathering of sediments in large tropical floodplains" (agreement 205DDEEES165). This is IPGP contribution 3876.

References

Abril, G., Martinez, J.-M., Artigas, L. F., Moreira-Turcq, P., Benedetti, L. Vidal, M. F., . . . Roland, F. (2014). Amazon River carbon dioxide outgassing fuelled by wetlands. *Nature*, *505*, 395–398.

Anderson, S. P., Dietrich, W. E., Torres, R., Montgomery, D. R., & Loague, K. (1997). Concentration-discharge relationships in runoff from a steep, unchanneled catchment. *Water Resources Research*, *33*(1), 211–225.

Aubert, A. H., Kirchner, J. W., Gascuel-Odoux, C., Faucheux, M., Gruau, G., & Mérot, P. (2013). Fractal water quality fluctuations spanning the periodic table in an intensively farmed watershed. *Environmental Science and Technology*, *48*(2), 930–937.

Aucour, A. M., Tao, F.-X., Moreira-Turcq, P., Seyler, P., Sheppard, S., & Benedetti, M. (2003). The Amazon River: Behaviour of metals (Fe, Al, Mn) and dissolved organic matter in the initial mixing at the Rio Negro/Solimoes confluence. *Chemical Geology*, *197*(1–4), 271–285.

Berner, R. A., Lasaga, A. C., & Garrels, R. M. (1983). The carbonate-silicate geochemical cycle and its effect on atmospheric carbon dioxide over the past 100 million years. *American Journal of Science*, *283*, 641–683.

Bluth, G. J. S., & Kump, L. R. (1994). Lithologic and climatologic controls of river chemistry. *Geochimica et Cosmochimica Acta*, *58*(10), 2341–2359.

Bouchez, J., Gaillardet, J., Lupker, M., Louvat, P., France-Lanord, C., Maurice, L., . . . Moquet, J. S. (2012). Floodplains of large rivers: Weathering reactors or simple silos? *Chemical Geology*, *332–333*, 166–184.

Bouchez, J., Lajeunesse, E., Gaillardet, J., France-Lanord, C., Dutra-Maia, P., & Maurice, L. (2010). Turbulent mixing in the Amazon river: The isotopic memory of confluence. *Earth and Planetary Science Letters*, *290*(1–2), 37–43.

Boy, J., Valarezo, C., & Wilcke, W. (2008). Water flow paths in soil control element exports in an Andean tropical montane forest. *European Journal of Soil Science*, *59*, 1209–1227.

Callède, J., Cochonneau, G., Ronchail, J., Vieira Alves, F., Guyot, J.-L., Santos Guimaraes, V., & De Oliveira, E. (2010). Les apports en eau de l'Amazone à l'océan Atlantique. *Revue Des Sciences De L'eau*, *23*(3).

Calmels, D., Galy, A., Hovius, N., Bickle, M., West, A. J., Chen, M. C., & Chapman, H. (2011). Contribution of deep groundwater to the weathering budget in a rapidly eroding mountain belt, Taiwan. *Earth and Planetary Science Letters*, *303*, 48–58.

Clow, D. W., & Mast, M. A. (2010). Mechanisms for chemostatic behavior in catchments: Implications for CO2 consumption by mineral weathering. *Chemical Geology*, *269*, 40–51.

Clymans, W., Govers, G., Frot, E., Ronchi, B., Van Wesemael, B., & Struyf, E. (2013). Temporal dynamics of bio-available Si fluxes in a temperate forested catchment (Meerdaal forest, Belgium). *Biogeochemistry*, *116*, 275–291.

Cochonneau, G., Sondag, F., Guyot, J.-L., Geraldo, B., Filizola, N., Fraizy, P., . . . Vauchel, P. (2006). L'Observatoire de Recherche en Environnement, ORE HYBAM sur les grands fleuves amazoniens = The Environmental Observation and Research project, ORE HYBAM, and the rivers of the Amazon basin. In *The Fifth FRIEND World Conference held Climate: Variability and Change—Hydrological Impacts* (Vol. 308). Havana, Cuba: IAHS.

Dai, A., & Trenberth, K. E. (2002). Estimates of freshwater discharge from continents: Latitudinal and seasonal variations. *Journal of Hydrometeorology*, *3*, 660–687.

Devol, A. H., Forsberg, B. R., Richey, J. E., & Pimentel, T. P. (1995). Seasonal variation in chemical distributions in the Amazon (Solimoes) River: A multiyear time series. *Global Biogeochemical Cycles*, *9*(3), 307–328.

Duffy, C., & Cusumano, J. (1998). A low-dimensional model for concentration-discharge dynamics in groundwater systems. *Water Resources Research*, *34*(9), 2235–2247.

Duffy, C., & Gelhar, L. W. (1985). A frequency domain approach to water quality modeling in groundwater: Theory. *Water Resources Research*, *21*(8), 1175–1184.

Duffy, C., & Gelhar, L. W. (1986). A frequency domain analysis of groundwater quality fluctuations: Interpretation of field data. *Water Resources Research*, *22(7)*, 1115–1128. https://doi.org/10.1029/WR022i007p01115

Edokpa, D. A., Evans, M. G., & Rothwell, J. J. (2015). High fluvial export of dissolved organic nitrogen from a peatland catchment with elevated inorganic nitrogen deposition. *Science of the Total Environment*, *532*, 711–722.

Eiriksdottir, E. S., Gislason, S. R., & Oelkers, E. H. (2013). Does temperature or runoff control the feedback between chemical denudation and climate? Insights from NE Iceland. *Geochimica et Cosmochimica Acta*, *107*, 65–81.

Espinoza, J. C., Chavez, S., Ronchail, J., Junquas, C., Takahashi, K., & Lavado, W. (2015). Rainfall hotspots over the southern tropical Andes: Spatial distribution, rainfall intensity and relations with large-scale atmospheric circulation. *Water Resources Research*, *51*, 3459–3475, https://doi.org/10.1002/2014WR016273

Espinoza, J. C., Guyot, J. L., Ronchail, J., Cochoneau, G., Filizola, N., Fraizy, P., . . . Vauchel, P. (2009b). Contrasting regional discharge evolution in the Amazon Basin. *Journal of Hydrology*, *375*, 297–311.

Espinoza, J. C., Ronchail, J., Guyot, J.-L., Filizola, N., Noriega, L., Lavado, W., . . . Romero, R. (2009a). Spatio - Temporal rainfall variability in the Amazon basin countries (Brazil, Peru, Bolivia, and Ecuador). *International Journal of Climatology*, *29*, 1574–1594.

Evans, C., & Davies, T. D. (1998). Causes of concentration/discharge hysteresis and its potential as a tool for analysis of episode hydrochemistr. *Water Resources Research*, *34*(1), 129–137.

Floury, P., Gaillardet, J., Gayer, É., Bouchez, J., Tallec, G., Ansart, P., Koch, F., . . . Roubaty, J.-L. (2017). The potamochemical symphony: New progresses in the high-frequency acquisition of stream chemical data. *Hydrological Earth System Science Discussions*, 2017.

Fraysse, F., Cantais, F., Pokrovsky, O. S., Schott, J., & Meunier, J. D. (2006). Aqueous reactivity of phytoliths and plant litter: Physico-chemical constraints on terrestrial biogeochemical cycle of silicon. *Journal of Geochemical Exploration*, *88*(1–3), 202–205.

Gaillardet, J., Dupré, B., Allègre, C.-J., & Négrel, P. (1997). Chemical and physical denudation in the Amazon River Basin. *Chemical Geology*, *142*(3-4), 141–173.

Gibbs, R. J. (1967). The geochemistry of the Amazon river system: Part I. The factors that control the salinity and the composition and concentration of the suspended Solids. *Geological Society of America Bulletin*, *78*, 1203–1232.
Goddéris, Y., François, L. M., Probst, A., Schott, J., Moncoulon, D., Labat, D., & Viville, D. (2006). Modelling weathering processes at the catchment scale: The WITCH numerical. *Geochimica et Cosmochimica Acta*, *70*, 1128–1147.
Godsey, S. E., Aas, W., Clair, T. A., de Wit, H. A., Fernandez, I. J., Kahl, J. S., . . . Kirchner, J. W. (2010). Generality of fractal 1/f scaling in catchment tracer time series, and its implications for catchment travel time distributions. *Hydrological Processes*, *24*(12), 1660–1671. https://doi.org/10.1002/hyp.7677
Godsey, S. E., Kirchner, J. W., & Clow, D. W. (2009). Concentration–discharge relationships reflect chemostatic characteristics of US catchments. *Hydrological Processes*, *23*, 1844–1864.
Guimberteau, M., Drapeau, G., Ronchail, J., Sultan, B., Polcher, J., Martinez, J.-M., . . . Vauchel, P. (2012). Discharge simulation in the subbasins of the Amazon using ORCHIDEE forced by new datasets. *Hydrology and Earth System Sciences*, *16*, 911–935.
Guinoiseau, D., Bouchez, J., Gélabert, A., Louvat, P., Filizola, N., & Benedetti, M. F. (2016). The geochemical filter of large river confluences. *Chemical Geology*, *441*, 191–203.
Guyot, J.-L. (1993). *Hydrogéochimie des fleuves de l'Amazonie Bolivienne*. Paris, France: ORSTOM.
Hornberger, G. M., Scanlon, T. M., & Raffensperger, J. P. (2001). Modelling transport of dissolved silica in a forested headwater catchment: The effect of hydrological and chemical time scales on hysteresis in the concentration–discharge relationship. *Hydrological Processes*, *15*, 2029–2038. https://doi.org/10.1002/hyp.254
House, W. A., & Warwick, M. S. (1998). Hysteresis of solute concentration/Discharge relationship in rivers during storms. *Water Resources Research*, *32*(8), 2279–2290.
Hughes, H., Sondag, F., Santos, R. V., André, L., & Cardinal, D. (2013). The riverine silicon isotope composition of the Amazon Basin. *Geochimica et Cosmochimica Acta*, *121*, 637–651.
Ibarra, D. E., Caves, J. K., Moon, S., Thomas, D. L., Hartmann, J., Chamberlain, C. P., & Maher, K. (2016). Differential weathering of basaltic and granitic catchments from concentration–discharge relationships. *Geochimica et Cosmochimica Acta*, *190*, 265–293.
Johnson, N., Likens, G., Bormann, F., Fisher, D., & Pierce, R. (1969). A working model for the variation in stream water chemistry at the Hubbard Brook Experimental Forest, New Hampshire. *Water Resources Research*, *5(6)*, 1353–1363.
Kirchner, J. W. (2016a). Aggregation in environmental systems – Part 1: Seasonal tracer cycles quantify young water fractions, but not mean transit times, in spatially heterogeneous catchments. *Hydrology and Earth System Sciences*, *20*, 279–297. https://doi.org/10.5194/hess-20-279-2016
Kirchner, J. W. (2016b). Aggregation in environmental systems – Part 2: Catchment mean transit times and young water fractions under hydrologic nonstationarity. *Hydrology and Earth System Sciences*, *20*, 299–328.
Kirchner, J. W., Feng, X., & Neal, C. (2000). Fractal stream chemistry and its implications for contaminant transport in catchments. *Nature*, *403*, 524–527.
Kirchner, J. W., Feng, X., & Neal, C. (2001). Fractal stream chemistry and its implications for contaminant transport in catchments. *Journal of Hydrology*, *254*, 81–100.
Kirchner, J. W., & Neal, C. (2013). Universal fractal scaling in stream chemistry and its implications for solute transport and water quality trend detection. *Proceedings of the National Academy of Sciences U. S. A.*, *110*(30), 12213–12218.
Konhauser, K. O., Mann, H., Fyfe, W. S., (1992). Prolific Organic SiO2 Precipitation in a Solute Deficient River: Rio Negro, Brazil. *Geology*, *20*, 227–230.
Langbein, W. B., & Dawdy, D. R. (1964). Occurrence of dissolved solids in surface waters. *U.S. Geological Survey Professional Papers*, *501–D*, D115–D117.
Laraque, A., Guyot, J.-L., & Filizola, N. (2009). Mixing processes in the Amazon River at the confluences of the Negro and Solimões rivers, Encontro das Aguas, Manaus, Brazil. *Hydrological Processes*, *23*, 31–40.
Latrubesse, E. M., Arima, E. Y., Dunne, T., Park, E., Baker, V. R., d'Horta, F. M., . . . Stevaux, J. C. (2017). Damming the rivers of the Amazon basin. *Nature*, *546*, 363–369.
Lucas, Y. (2001). The role of plants in controlling rates and products of weathering: Importance of biological pumping. *Annual Reviews of Earth and Planetary Sciences*, *29*, 135–163.
Maher, K. (2010). The dependence of chemical weathering rates on fluid residence time. *Earth and Planetary Science Letters*, *294*, 101–110.
Maher, K. (2011). The role of fluid residence time and topographic scales in determining chemical fluxes from landscapes. *Earth and Planetary Science Letters*, *312*, 48–58.
Maher, K., & Chamberlain, C. P. (2014). Hydrologic regulation of chemical weathering and the geologic carbon cycle. *Science*, *343*, 1502–1504.
Marengo, J., Liebmann, B., Grimm, A. M., Misra, V., Silva Dias, P. L., Cavalcanti, I. F. A., . . . Alves, L. M. (2012). Review - Recent developments on the South American monsoon system. *International Journal of Climatology*, *32*, 1–21.
Markewitz, D., Davidson, E. A., Figueiredo, R. D. O., Victoria, R. L., & Krusche, A. V. (2001). Control of cation concentrations in stream waters by surface soil processes in an Amazonian watershed. *Nature*, *410*, 802–805.
Meybeck, M. (1976). Total mineral dissolved transport by world major rivers/Transport en sels dissous des plus grands fleuves mondiaux. *Hydrological Sciences Bulletin*, *21*(2), 265–284.
Molina-Carpio, J., Espinoza, J. C., Vauchel, P., Ronchail, J., Gutierrez Caloir, B., Guyot, J.-L., & Noriega, L. (2017). Hydroclimatology of the Upper Madeira River basin: Spatio-temporal variability and trends. *Hydrological Sciences Journal*, *62*, 1–17. https://doi.org/10.1080/02626667.2016.1267861
Moon, S., Chamberlain, C. P., & Hilley, G. E. (2014). New estimates of silicate weathering rates and their uncertainties in global rivers. *Geochimica et Cosmochimica Acta*, *134*, 257–274.
Moquet, J.-S., Crave, A., Viers, J., Seyler, P., Armijos, E., Bourrel, L., . . . Guyot, J.-L. (2011). Chemical weathering and atmospheric/soil CO2 uptake in the Andean and Foreland Amazon basins. *Chemical Geology*, *287*(1–2), 1–26.
Moquet, J. S., Guyot, J.-L., Crave, A., Viers, J., Filizola, N., Martinez, J.-M., . . . Pombosa, R. (2016). Amazon River dissolved load: Temporal dynamic and annual budget from the Andes to the ocean. *Environmental Science and Pollution Research*, *23*(12), 11405–11429. https://doi.org/10.1007/s11356-015-5503-6
Moquet, J. S., Maurice, L., Crave, A., Viers, J., Aravelo, N., Lagane, C., . . . Guyot, J. L. (2014b). Cl and Na fluxes in an Andean foreland basin of the Peruvian Amazon: An anthropogenic impact evidence. *Aquatic Geochemistry*, *20*(6), 613–637.
Moquet, J. S., Viers, J., Crave, A., Armijos, E., Lagane, C., Lavado, W., . . . Guyot, J.-L. (2014a). Comparison between silicate weathering and physical erosion rates in Andean basins of Amazon river. *Procedia Earth & Planetary Science*, *10*, 275–279.
Moulton, K., West, J., & Berner, R. A. (2000). Solute flux and mineral mass balance approaches to the quantification of plant effects on silicate weathering. *American Journal of Sciences*, *300*, 539–570.

Neal, C., Neal, M., Reynolds, B., Maberly, S. C., May, L., Ferrier, R. C., . . . Parker, J. E. (2005). Silicon concentrations in UK surface waters. *Journal of Hydrology*, *304*, 75–93.

Neal, J., Schumann, G., & Bates, P. (2012). A subgrid channel model for simulating river hydraulics and floodplain inundation over large and data sparse areas. *Water Resources Research*, *48*, W11506. https://doi.org/10.1029/2012WR012514

Ollivier, P., Radakovitch, O., & Hamelin, B. (2006). Unusual variations of dissolved As, Sb and Ni in the Rhône River during flood events. *Journal of Geochemical Exploration*, *88*, 394–398.

Rios-Villamizar, E. A., Piedade, M. T. F., da Costa, J. G., Adeney, J. M., & Junk, W. J. (2014). Chemistry of different Amazonian water types for river classification: A preliminary review. *WIT Transactions on Ecology and the Environment*, *178*, https://doi.org/10.2495/13WS 0021

Roche, M. A., & Fernandez, J. C. (1988). Water resources, salinity and salt yields of the rivers of the Bolivian Amazon. *Journal of Hydrology*, *101*, 305–331.

Rose, S. (2003). Comparative solute –discharge hysteresis analysis for an urbanized and a "control basin" in the Georgia (USA) Piedmont. *Journal of Hydrology*, *284*, 45–56.

Sanchez, L. S. H., Horbe, A., Moquet, J., Sondag, S. F., & Guyot, J. L. (2015). Variação espaço-temporal do material inorgânico dissolvido na bacia Amazônica. *Acta Amazonica*, *45*(2).

Saunders, J. F., & Lewis, W. M. (1989). Transport of major solutes and relationship between solute concentrations en discharge in the Apure River, Venezuela. *Biogeochemisrty*, *8*, 101–113.

Sioli, H. (1964). General features of the limnology of Amazonia. *Verhandlungen des Internationalen Verein Limnologie*, 15, 1053–1058.

Stallard, R. F., & Edmond, J. M. (1983). Geochemistry of the Amazon. 2. The influence of geology and weathering environment on the dissolved load. *Journal of Geophysical Research*, *88*(C14), 9671–9688.

Steefel, C. I., DePaolo, D. J., & Lichtner, P. C. (2005). Reactive transport modeling: An essential tool and new research approach for the Earth sciences. *Earth and Planetary Science Letters*, *240*, 539–558.

Torres, M. A., West, A. J., & Clark, K. E. (2015). Geomorphic regime modulates hydrologic control of chemical weathering in the Andes–Amazon. *Geochimica et Cosmochimica Acta*, *166*, 105–128.

Vauchel, P. (2005). HYDRACCESS: Software for Management and processing of Hydro - meteorological data. Retrieved from www.mpl.ird.fr/hybam/outils/hydraccess

Vera, C., Higgins, W., Amador, J., Ambrizzi, T., Garreaud, R., Gochis, D., . . . Zhang, C. (2006). Toward a unified view of the American Monsoon Systems. *American Meteorological Society*, *19*, 4977–5000.

Von Blanckenburg, F., Bouchez, J., Ibarra, D. E., & Maher, K. (2015). Stable runoff and weathering fluxes into the oceans over Quaternary climate cycles. *Nature Geosciences*, *8*, 538–542. https://doi.org/10.1038/NGEO2452

Wittmann, H., von Blanckenburg, F., Maurice, L., Guyot, J.-L., Filizola, N., & Kubik, P. W. (2011). Sediment production and delivery in the Amazon River basin quantified by in situ-produced cosmogenic nuclides and recent river loads. *Geological Society of America Bulletin*, *123*(5-6), 934–950.